

Reducing the Model Error of the Graphical Methods for Volume of Distribution Measurements in PIB-PET study

Hongbin Guo^{*,a}, Rosemary A Renaut^a, Kewei Chen^b, Eric M Reiman^b

^aArizona State University, School of Mathematical and Statistical Sciences, Tempe, AZ 85287-1804.

^bBanner Alzheimer Institute and Banner Good Samaritan Positron Emission Tomography Center, Phoenix, AZ 85006

Abstract

Graphical analysis methods are widely used in positron emission tomography quantification because of their simplicity and model independence. But they may, particularly for reversible kinetics, lead to bias in the estimated parameters. The source of the bias is commonly attributed to noise in the data. Assuming a two-tissue compartmental model, we investigate the bias that originates from model error. This bias is an intrinsic property of the simplified linear models used for limited scan durations, and it is exaggerated by random noise and numerical quadrature error. Conditions are derived under which Logan's graphical method either over- or under-estimates the distribution volume in the noise-free case. The bias caused by model error is quantified analytically. The presented analysis shows that the bias of graphical methods is inversely proportional to the dissociation rate. Furthermore, visual examination of the linearity of the Logan plot is not sufficient for guaranteeing that equilibrium has been reached. A new model which retains the elegant properties of graphical analysis methods is presented, along with a numerical algorithm for its solution. We perform simulations with the fibrillar amyloid β radioligand [11C] benzothiazole-aniline using published data from the University of Pittsburgh and Rotterdam groups. The results show that the proposed method significantly reduces the bias due to model error. Moreover, the results for data acquired over a 70 minutes scan duration are at least as good as those obtained using existing methods for data acquired over a 90 minutes scan duration.

Key words: Bias; graphical analysis; Logan plot; PET quantification; PIB; Alzheimer's disease; distribution volume.

PACS: 82.20.Wt, 87.57.-s, 87.57.uk

1. Introduction

Graphical analysis (GA) has been routinely used for quantification of positron emission tomography (PET) radioligand measurements. These techniques have been utilized both with input data acquired from plasma measurements and using the time activity curve from a reference brain region. They have been used for calculation of tracer uptake rates, absolute volumes of distribution (V_T) and distribution volume ratios (DVR), or, equivalently, for binding potentials (BP_{ND} , BP_F and BP_P). They are widely used because of their inherent simplicity and general applicability regardless of the specific compartmental model.

The well-known bias, particularly for reversible kinetics, in parameters estimated by GA is commonly attributed to noise in the data, [1, 2, 3], and therefore techniques to reduce the bias have concentrated on

*Corresponding author. Tel: 1-480-965-8002, Fax: 1-480-965-4160.

Email address: hb_guo@asu.edu (Hongbin Guo)

limiting the impact of the noise, [4, 5, 6, 7, 2, 8, 9]. . Here, we turn our attention to another important source of the bias: the model error which is implicit in GA approaches.

The bias associated with GA approaches has, we believe, three possible sources. The bias arising due to random noise is most often discussed, but errors may also be attributed to the use of numerical quadrature and an approximation of the underlying compartmental model. It is demonstrated in Section 2 that not only is bias an intrinsic property of the linear model for limited scan durations, which is exaggerated by noise, but also that it may be dominated by the effects of the model error. Indeed, numerical simulations, presented in Section 4, demonstrate that large bias can result even in the noise-free case. Conditions for over- or under-estimation of the V_T due to model error and the extent of bias of the Logan plot are quantified analytically. These lead to the design of a bias correction method, Section 3, which still maintains the elegant simplicity of GA approaches. This bias reduction is achieved by the introduction of a simple nonlinear term in the model. While this approach adds some moderate computational expense, simulations reported in Section 4.3 for the fibrillar amyloid β radioligand [11C] benzothiazole-aniline (Pittsburgh Compound-B [PIB]), [10], illustrate that it greatly reduces bias. Relevant observations are discussed in Section 5 and conclusions presented in Section 6. The necessary mathematical analyses are presented in *Appendices*.

2. Theory

2.1. Existing linear methods

For the measurement of V_T , existing linear quantification methods for reversible radiotracers with a known input function, i.e. the unmetabolized tracer concentration in plasma, are based on the following linear approximation of the true kinetics, [11]:

$$\text{MA0 : } \int_0^t C_T(\tau) d\tau \approx V_T \int_0^t C_P(\tau) d\tau - b C_T(t). \quad (1)$$

Here $C_T(t)$ is the measured *tissue time activity curve* (TTAC), $C_P(t)$ is the *input function*, V_T represents the *volume of distribution* and quantity b is a constant. With known $C_T(t)$ and $C_P(t)$ we can solve for V_T and b by the method of linear least squares. This model, which we denote by MA0 to distinguish it from MA1 and MA2 introduced in [2], approximately describes tracer behavior at equilibrium. Dividing through by $C_T(t)$, showing that the V_T is the linear slope and $-b$ the intercept, yields the original Logan graphical analysis model, denoted here by Logan-GA,

$$\text{Logan - GA : } \frac{\int_0^t C_T(\tau) d\tau}{C_T(t)} \approx V_T \frac{\int_0^t C_P(\tau) d\tau}{C_T(t)} - b, \quad (2)$$

in which the V_T and intercept $-b$ are obtained by using linear least squares (LS) for the sampled version of (2). Although it is well-known that this model often leads to under-estimation of the V_T it is still widely used in PET studies. An alternative formulation based on (1) is the MA1,

$$\text{MA1 : } C_T(t) \approx \frac{V_T}{b} \int_0^t C_P(\tau) d\tau - \frac{1}{b} \int_0^t C_T(\tau) d\tau, \quad (3)$$

for which the V_T can again be obtained using LS [2]. The focus here is thus examination of the model error specifically for Logan-GA and MA1, from which a new method for reduction of model error is designed.

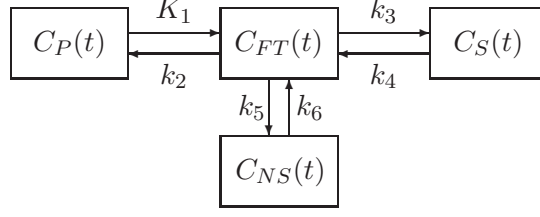


Figure 1: Three-tissue compartmental model of reversible radioligand binding dynamics.

2.2. Model error analysis

The general three-tissue compartmental model for the reversible radioligand binding kinetics of a given brain region or a voxel is illustrated in Figure 1, [12, 13]:

Here $C_P(t)$ ($kBq \cdot mL^{-1}$) is the input function, i.e. the unmetabolized radiotracer concentration in plasma, and $C_{FT}(t)$, $C_{NS}(t)$ and $C_S(t)$ ($kBq \cdot mL^{-1}$) are free radioactivity, nonspecific bound and specific bound tracer concentrations, resp., and K_1 ($mL \cdot mL^{-1} \cdot min^{-1}$) and k_i (min^{-1}), $i = 2, \dots, 6$, are rate constants. The V_T is related to the rate constants as follows [14],

$$V_T = \frac{K_1}{k_2} \left(1 + \frac{k_3}{k_4} + \frac{k_5}{k_6} \right). \quad (4)$$

The numerical implementation for estimating the unknown rate constants of the differential system illustrated in Figure 1 is difficult because three exponentials are involved in the solution of this system, [13]. Specifically, without the inclusion of additional prior knowledge, the rate constants may be unidentifiable, [15]. Fortunately, for most tracers it can safely be assumed that C_{NS} and C_{FT} reach equilibrium rapidly for specific binding regions. Then it is appropriate to use a two-tissue four-parameter (2T-4k) model by binning $C_{NS}(t)$ and $C_{FT}(t)$ to one compartment $C_{ND}(t) = C_{FT}(t) + C_{NS}(t)$. This is equivalent to taking $k_5 = k_6 = 0$, and hence $C_{NS}(t) = 0$. On the other hand, for regions without specific binding activity, we know $C_S(t) = 0$ which is equivalent to taking $k_3 = k_4 = 0$. For some tracers, however, for example the modeling of PIB in the cerebellar reference region, the best data fitting is obtained by using the 2T-4k model without binning $C_{NS}(t)$ and $C_{FT}(t)$, [16]. Assuming the latter, the V_T is given by $K_1/k_2(1 + k_3/k_4)$, and $K_1/k_2(1 + k_5/k_6)$, for regions with and without specific binding activity, resp. Ignoring the notational differences between the two models, for regions with and without specific binding activity, they are both described by the same abstract mathematical 2T-4k model equations. Here, without loss of generality, we present the 2T-4k model equations for specific binding regions,

$$\frac{dC_{ND}(t)}{dt} = K_1 C_P(t) - (k_2 + k_3) C_{ND}(t) + k_4 C_S(t) \quad (5)$$

$$\frac{dC_S(t)}{dt} = k_3 C_{ND}(t) - k_4 C_S(t). \quad (6)$$

To obtain the equations appropriate for regions without specific binding activity, $C_S(t)$ is replaced by $C_{NS}(t)$ and k_3 and k_4 are interpreted as the association and dissociation parameters of regions without specific binding activity. To simplify the explanation $C_S(t)$, k_3 and k_4 are used throughout for both regions with and without specific binding activity, with the assumption that $C_S(t)$, k_3 and k_4 should automatically be replaced by $C_{NS}(t)$, k_5 and k_6 respectively, when relevant.

The solution of the linear differential system (5)-(6) is given by

$$C_{ND}(t) = (a_1 e^{-\alpha_1 t} + b_1 e^{-\alpha_2 t}) \otimes C_P(t) \quad (7)$$

$$C_S(t) = a_2 (e^{-\alpha_1 t} - e^{-\alpha_2 t}) \otimes C_P(t) \quad (8)$$

where \otimes represents the convolution operation,

$$\begin{aligned} \alpha_{1,2} &= (k_2 + k_3 + k_4 \mp \sqrt{(k_2 + k_3 + k_4)^2 - 4k_2k_4})/2, \quad \text{and} \\ a_1 &= \frac{K_1(k_4 - \alpha_1)}{\alpha_2 - \alpha_1}, \quad b_1 = \frac{K_1(\alpha_2 - k_4)}{\alpha_2 - \alpha_1}, \quad \text{and } a_2 = \frac{K_1k_3}{\alpha_2 - \alpha_1}. \end{aligned} \quad (9)$$

The overall concentration of radioactivity is

$$C_T(t) = C_{ND}(t) + C_S(t) = ((a_1 + a_2)e^{-\alpha_1 t} + (b_1 - a_2)e^{-\alpha_2 t}) \otimes C_P(t). \quad (10)$$

Integrating (5)-(6) and rearranging, details are presented in Appendix C, yields

$$\int_0^t C_T(\tau) d\tau = V_T \int_0^t C_P(\tau) d\tau - \frac{k_3 + k_4}{k_2 k_4} C_{ND}(t) - \frac{k_2 + k_3 + k_4}{k_2 k_4} C_S(t), \quad (11)$$

$$= V_T \int_0^t C_P(\tau) d\tau - \frac{k_3 + k_4}{k_2 k_4} C_T(t) - \frac{1}{k_4} C_S(t). \quad (12)$$

This is model (1) when $C_S(t)$ is linearly proportional to $C_T(t)$ for a time window within the scan duration of T minutes. The accuracy of linear methods based on (1) is thus dependent on the validity of the assumption that $C_S(t)$ and $C_{ND}(t)$ are approximately linearly proportional to $C_T(t)$ over a time window within $[0, T]$. Logan observed that $C_{ND}(t)$ and $C_S(t)$ are roughly proportional to $C_T(t)$, after some time point t^* , [11]. If the assumption of linear proportionality breaks down for the given window, $[t^*, T]$, model error will be introduced to the estimated uptake rate or V_T , as shown later in Section 4.3. Indeed, in Section 5.1 we show that, for the PIB radioligand on some regions with small k_4 , there is no window within a 90 minutes scan duration where $C_S(t)$ and $C_T(t)$ are linearly proportional. This is despite the apparent good linearity, visually, of the Logan plot of $\int_0^t C_T(\tau) d\tau / C_T(t)$ against $\int_0^t C_P(\tau) d\tau / C_T(t)$. Waiting for equilibrium, which may take several hours, is impractical in terms of patient comfort, cost and measurement of radioactivities.

The limitation of the constant approximation can be analysed theoretically. We assume $\alpha_2 \gg \alpha_1 > 0$ and $C_P(t)$ is very small for large time, which is the case for PIB and most other tracers, then the convolution $e^{-\alpha_2 t} \otimes C_P(t) = \int_0^t e^{-\alpha_2(t-\tau)} C_P(\tau) d\tau$ is relatively small. Thus we can safely assume that the ratio of $e^{-\alpha_2 t} \otimes C_P(t)$ to $e^{-\alpha_1 t} \otimes C_P(t)$ is roughly 0 for $t > t^*$. Consequently, $C_S(t)$, see equation (8), can be approximated by $a_2 e^{-\alpha_1 t} \otimes C_P(t)$ for $t > t^*$. In our tests with PIB, the neglected component $a_2 e^{-\alpha_2 t} \otimes C_P(t)$ is less than 8% $C_S(t)$ for $t \geq 35$ min.. On the other hand, this is not the case for $C_{ND}(t)$, see equation (7), because a_1 and b_1 need not be of the same scale. For example, if $k_4 \ll k_2 + k_3$ we know $b_1/a_1 \approx (k_2 + k_3)/(2k_4)$ from (9), thus $b_1 \gg a_1 > 0$. Specifically, $b_1 e^{-\alpha_2 t} \otimes C_P(t)$ may not be small in relation to $a_1 e^{-\alpha_1 t} \otimes C_P(t)$. This means $C_S(t)$ may not be proportional to $C_{ND}(t)$ for $t \in [t^*, T]$. Thus, it is not appropriate, as is assumed for the Logan-GA (2) and other linear methods derived from MA0, to approximate

$$\bar{s}(t) = \frac{k_3 + k_4}{k_2 k_4} \cdot \frac{C_{ND}(t)}{C_T(t)} + \frac{k_2 + k_3 + k_4}{k_2 k_4} \cdot \frac{C_S(t)}{C_T(t)} = \frac{k_3 + k_4}{k_2 k_4} + \frac{1}{k_4} C_S(t)/C_T(t), \quad (13)$$

as constant for $t \in [t^*, T]$. One may argue that if $(a_1 + a_2)/(b_1 - a_2)$, which is less than one, is close to 1 the term $e^{-\alpha_2 t} \otimes C_P(t)$ in $C_T(t)$ could be ignored. Then the ratio of $C_T(t)$ to $C_S(t)$ would be close to constant after t^* , and the resulting estimates of the V_T using Logan-GA (2) and MA1 (3) would be reasonable. While it is easy to verify that $(a_1 + a_2)/(b_1 - a_2)$ is positive and bounded above by one, this fraction need not be close to its upper bound. Indeed, for realistic test data, see Table 1, $0.05 \leq (a_1 + a_2)/(b_1 - a_2) \leq 0.65$. The simulations presented in Tables 2 and 3 validate that a small value of this fraction may cause a problem in the estimation of the V_T using the linear Logan-GA and MA1 methods.

2.3. Model error of Logan equation

Mathematical details concerning the model error of Logan-GA and MA0 are presented in Appendices and similar results, omitted here to save space, can be obtained for MA1. We summarize in the following theorem, for which the main idea is to show that replacing (13) which occurs on the right hand side of (11) by a constant intercept b introduces an error in the least squares solution for the V_T which can be specifically quantified.

Theorem 1. *Assume the noise-free instantaneous measurements for both C_T and input function are known and follow the 2-tissue model, the C_T does not have contamination from vascular activity, the linear least squares is used for Logan-GA and MA0 calculation, and the noise-free sample data has n frames with frame time $t_i, i = 1, \dots, n$. Let $t^* = t_l$ and $m = n - l + 1$. Then, with $\bar{s}(t)$ as defined in (13), for each method the same conclusions are reached:*

- *The V_T is over-estimated (under-estimated) if $\bar{s}(t), t \in [t_l, t_n]$, is a non-constant decreasing (increasing) function, and*
- *the V_T is exact if $\bar{s}(t), t \in [t_l, t_n]$, is a constant function;*

Let V_T^{true} be the true value of the V_T , then the error in V_T^{Logan} calculated by Logan-GA is bounded by

$$|V_T^{\text{Logan}} - V_T^{\text{True}}| \leq \phi D, \quad (14)$$

where D is the difference between the largest and the smallest values of $\bar{s}(t)$ in $[t_l, t_n]$, i.e. D reflects the flatness of $\bar{s}(t)$ in $[t_l, t_n]$. The quantity ϕ is defined as follows

$$\phi = \frac{m \sum_{i=l}^n \bar{\mathbf{p}}_i}{m \sum_{i=l}^n \bar{\mathbf{p}}_i^2 - \left(\sum_{i=l}^n \bar{\mathbf{p}}_i \right)^2},$$

in which $\bar{\mathbf{p}}_i = \int_0^{t_i} C_P(\tau) d\tau / C_T(t_i)$.

This theorem is an immediate result of Lemma 3 and Corollary 2 (*Appendix A*) for the vectors obtained from the sampling of the functions

$$\mathbf{s}(t) = \frac{k_3 + k_4}{k_2 k_4} C_{ND}(t) + \frac{k_2 + k_3 + k_4}{k_2 k_4} C_S(t), \quad \text{and}$$

$$\mathbf{r}(t) = \int_0^t C_T(\tau) d\tau, \quad \mathbf{p}(t) = \int_0^t C_P(\tau) d\tau, \quad \mathbf{q}(t) = C_T(t),$$

at discrete time points $t = t_l, \dots, t_n$. The relevant vectors are defined by $\bar{\mathbf{r}} = \mathbf{r}/\mathbf{q}$, $\bar{\mathbf{p}} = \mathbf{p}/\mathbf{q}$, $\bar{\mathbf{s}} = \mathbf{s}/\mathbf{q}$, where the division corresponds to componentwise division. It is easy to check that all these vectors are positive vectors, \mathbf{p} , $\bar{\mathbf{p}}$, \mathbf{r} and $\bar{\mathbf{r}}$ are non-constant increasing vectors and \mathbf{q} is decreasing. Thus all conditions for Lemma 3 and Corollary 2 are satisfied. In the latter discussion we may use the variation (increasing or decreasing) of $C_S(t)/(k_4 C_T(t))$ instead of that of $\bar{s}(t)$ because of (13).

It is not surprising that the properties of Logan-GA and MA0 are similar. Indeed, MA0 is none other than weighted Logan-GA with weights $C_T(t_i)$, which changes the noise structure in the variables. In contrast to the conventional under-estimation observations, it is surprising that the V_T may be over-estimated. However, the over-estimation is indeed observed in the tests presented in Section 4.2 and 4.3. Inequality (14) indicates that Logan-type linear methods will work well for data for which \bar{s} is flat.

Unfortunately, \bar{s} may become flat only for a late time interval. **Thus our interest, in Section 3, is to better estimate the V_T using a reasonable (practical) time window, which may include the window over which $C_S(t)/C_T(t)$ is still increasing.** Our initial focus is on the modification of Logan-type methods. Then, in Section 4 we present numerical simulations using noise-free data which illustrate the difficulties with Logan-GA and MA1, and support the results of Theorem 1.

3. Methods

In the previous discussion we have seen the theoretical limitations of the Logan-GA and MA1 methods. Here we present a new model and associated algorithm which assists with reducing the bias in the estimation of the V_T .

Observe that, the assumption $\alpha_2 \gg \alpha_1$, implies that $C_S = a_2 e^{-\alpha_1 t} \otimes C_P(t) + \epsilon(t)$, where $\epsilon(t)$ can be ignored for $t > t^*$. Therefore, for $t > t^*$ (12) can be approximated by a new model as follows

$$\int_0^t C_T(\tau) d\tau \approx V_T \int_0^t C_P(\tau) d\tau - AC_T(t) - Be^{-\alpha_1 t} \otimes C_P(t), \quad (15)$$

where $A = (k_3 + k_4)/k_2 k_4$ and $B = a_2/k_4$. This suggests new algorithms should be developed for estimation of parameters V_T , A , B and α_1 . Here, a new approach, based on the basis function method (BFM) in [17], in which α_1 is discretized, is given by the following Algorithm.

Algorithm 1. *Given $C_P(t_i)$ and $C_T(t_i)$ for $i = 1, \dots, n$ and $t^* = t_l$, the V_T is estimated by performing the following steps.*

1. Calculate V_T and intercept $-b$, using Logan-GA.
2. Set $\alpha_1^{\min} = 0.001$ and $\alpha_1^{\max} = \min(1, 2/b)$ if $b > 0$ otherwise $\alpha_1^{\max} = 1$.
3. Form discretization $\alpha_1^{(j)}$, $j = 1 : 100$ for α_1 , with equal spacing logarithmically between α_1^{\min} and α_1^{\max} .
4. For each j solve the linear LS problem, i.e. cast it as a multiple linear regression problem with $\int_0^t C_T(\tau) d\tau$ as the dependent variable.

$$V_T \int_0^t C_P(\tau) d\tau - AC_T(t) - B \int_0^t e^{-\alpha_1^{(j)} \tau} C_P(t - \tau) d\tau \approx \int_0^t C_T(\tau) d\tau \quad (16)$$

with data at t_i , $i = l, \dots, n$, to give values $V_T^{(j)}$, $A^{(j)}$ and $B^{(j)}$.

5. Determine $\alpha_1^{(j^*)}$ for which residual is minimum over all j . Set V_T , A and B to be $V_T^{(j^*)}$, $A^{(j^*)}$ and $B^{(j^*)}$, resp.

Remarks:

1. This algorithm is designed for the cases when $\alpha_2 \gg \alpha_1$. It focus on the model error correction as the title of this paper indicated, other error sources, e.g. data noise and plasma data resampling error, are accumulated to additive Gaussian noise and treated by least squares. More careful investigations on other error sources are needed to generate more accurate algorithms. Our initial work was shown in [18].
2. The interval for α_1 is determined as follows: First the lower bound 0.001 for α_1 is suitable for most tracers, but could be reduced appropriately. This lower bound is not the same as that on θ used in BFM, in which θ is required to be greater than the decay constant of the isotope, [17]. Second by point (2) of Corollary 2 (*Appendix A*, b should be positive and near the average value of $\bar{s}(t)$, where,

by (13), $\frac{k_3+k_4}{k_2k_4} < \bar{s}(t) < \frac{k_2+k_3+k_4}{k_2k_4}$. On the other hand, $\frac{k_2+k_3+k_4}{k_2k_4} \approx \frac{1}{\alpha_1}$ if $4k_2k_4$ is small relative to $(k_2 + k_3 + k_4)^2$. Thus, α_1 is linked with b through $\bar{s}(t)$. This is used to give the estimate of the upper bound on α_1 . Practically, it is possible that the Logan-GA may yield an intercept $b < 0$, then we set $\alpha_1^{\max} = 1$.

3. This algorithm extracts multiple parameters from the time activity curve, however, it does not increase variance while significantly reduce the bias of V_T , (no guarantee for A and B), as shown in our experiments. Numerically, because $\int_0^t C_P(\tau)d\tau$ is much larger than both $C_T(t)$ and $C_S(t)$ for $t > t^*$, the estimate of V_T is much more robust to noise in the formulation, including both model and random noise effects, than are the estimates of A and B . Therefore, while A and B may not be good estimates of $(k_3 + k_4)/(k_2k_4)$ and a_2/k_4 , resp. for noisy data, the estimate of V_T will still be acceptable. Details of the robust analysis, i.e. sensitivity to noise in the data, are presented in Appendix B.
4. The algorithm can be accelerated by employing a coarse-to-fine multigrid strategy. The coarser level grid provides bounds for the fine level grid. The grid resolution can be gradually refined until the required accuracy is satisfied.

4. Experimental Results

We present a series of simulations which first validate the theoretical analysis of Section 2 for noise-free data, and then numerical experiments which contrast the performance of Algorithm 1 with Logan-GA, MA1 and nonlinear kinetic analysis (KA) algorithms for noisy data.

4.1. Simulated Noise-Free Data

We assume the radioligand binding system is well modeled by the 2T-4k compartmental model and focus the analysis on the bias in the estimated V_T which can be attributed to the simplification of the 2T-4k model. For the simulation we use representative kinetic parameters for brain studies with the PIB tracer. These kinetic parameters, detailed in Table 1, are adopted from published clinical data, [16, 19]. The simulated regions include the posterior cingulate (PCG), cerebellum (Cere) and a combination of cortical regions (Cort). The kinetic parameters of each ROI are also associated with the subject medical condition, namely normal controls (NC) and Alzheimer's Disease (AD) diagnosed subjects. The kinetic parameters for the first seven ROIs are from [16] while the last four are from [19]. Rate constants for ROIs **5** to **11** are directly adopted from the published literature, while those for ROIs **1** to **4** are rebuilt from information provided in [16]. The values for ROIs **1** to **4** and **8** to **11** represent average values for each group, while those for ROIs **5** and **6** are derived from one AD subject and those for ROI **7** from another AD subject.

The noise-free decay-corrected input function is adapted from the plasma measurements for a NC subject as presented in Figure 3(A) of [16]. Using the data from that figure we convert to $kBq \cdot mL^{-1}$ under the assumption of a 100kg body mass, and obtain the functional representation for $C_P(t) = u(t)$, ($kBq \cdot mL^{-1}$), which is illustrated in Figure 2:

$$u(t) = \begin{cases} 0 & t \in [0, 0.3] \\ 407.4933(t - 0.3) & t \in [0.3, 0.6] \\ -436.6t + 384.208 & t \in [0.6, 0.76] \\ 46.6747(t + 0.24)^{-2.2560} + 5.7173(t + 0.24)^{-0.5644} & t \geq 0.76. \end{cases} \quad (17)$$

Using this input function and the eleven data sets given in Table 1 eleven noise-free TTACS, $C_T(t)$ ($kBq \cdot mL^{-1}$), are generated using the 2T-4k model. The scanning protocol, consistent with that adopted in [16], has frame durations, Δt_i , measured in minutes, 4×0.25 , 8×0.5 , 9×1 , 2×3 , 8×5 and 3×10 .

Table 1: Rate constants for eleven ROIs, including PCG, Cere, and Cort, for AD and NC adopted from [16, 19]. For ROIs **6**, **7**, **10** and **11** no specific binding activity is assumed, i.e. $k_3 = k_4 = 0$, $V_T = K_1/k_2(1 + k_5/k_6)$; while for ROIs **1** to **5**, **8** and **9** we assume that the free and nonspecific compartments rapidly reach equilibrium, i.e. $k_5 = k_6 = 0$, $V_T = K_1/k_2(1 + k_3/k_4)$. Coefficients a_1 , b_1 and a_2 are defined in (9). The values for ROIs **1** to **4** and **8** to **11** represent average values for each group, while those for ROIs **5** and **6** are derived from one AD subject and those for ROI **7** from another AD subject.

ROI/Group	Area	K_1	k_2	k_3	k_4	k_5	k_6	V_T	$\frac{a_1+a_2}{b_1-a_2}$
1/NC	Cort	0.250	0.152	0.015	0.0106	0	0	3.9722	0.11
2/AD	Cort	0.220	0.113	0.056	0.023	0	0	6.6872	0.65
3/NC	PCG	0.250	0.150	0.015	0.0106	0	0	4.0252	0.11
4/AD	PCG	0.220	0.100	0.050	0.017	0	0	8.6706	0.63
5/AD	PCG	0.262	0.121	0.044	0.015	0	0	8.5168	0.44
6/AD	Cere	0.273	0.144	0	0	0.007	0.005	4.5500	0.05
7/AD	Cere	0.333	0.172	0	0	0.029	0.042	3.2728	0.26
8/NC	Cort	0.250	0.140	0.020	0.018	0	0	3.7480	0.18
9/AD	Cort	0.220	0.110	0.050	0.025	0	0	5.9841	0.63
10/NC	Cere	0.270	0.140	0	0	0.020	0.026	3.4353	0.20
11/AD	Cere	0.260	0.130	0	0	0.020	0.025	3.5810	0.22

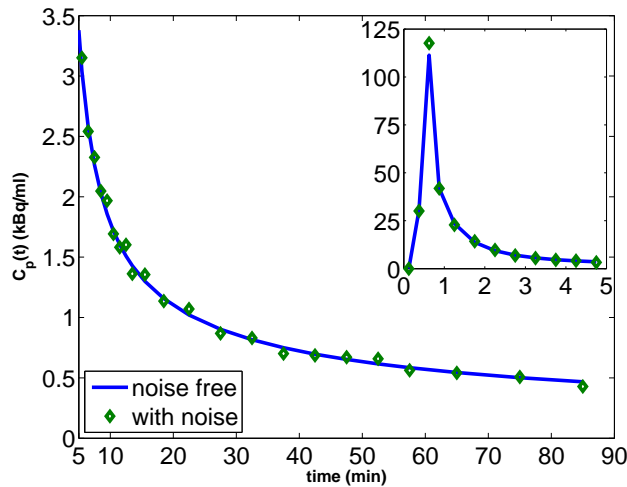


Figure 2: The true input function as given by (17), and the simulated measurements with noise. The simulated measurements are generated by (19) with $CV_S = 0.05$, $e = 50\%$, $\mu = 0.5\text{ml}$ and $\Delta w_i = 100$ seconds. The function over the initial 5 minutes is illustrated in the inset.

The last eight frames, which fall in the window from 35 to 90 minutes, are chosen for the time window over which we assume that equilibrium is achieved. A scan duration of 90 minutes is common for most PIB-PET dynamic studies, [20].

4.2. Examples of over-estimation for Logan-GA and MA1

Theorem 1 predicts that the V_T will be over-estimated when \bar{s} decreases. This is validated for data for the simulated ROIs. The estimates of the V_T , for scan durations $T = 90$ minutes with $t^* = 35$ minutes, and $T = 240$ minutes with $t^* = 100$ minutes, are reported in Table 2. The extended time window is generated by adding 15 frames each of 10 minutes length. Indeed, the over-estimation predicted in Theorem 1 is confirmed for ROI 7, for which the decrease of $C_S(t)/C_T(t)$ and, hence \bar{s} after 35 minutes, is clearly illustrated in Figure 5. Moreover, $C_S(t)/C_T(t)$ is decreasing after 100 minutes for all ROIs except ROI 6, see Figure 5(b), and in all but this case the values of V_T are over-estimated. We note that \bar{s} is nearly flat on the selected windows, $[t^*, T]$ for the cases in which the over-estimation of V_T is small. These results further validate the conclusions of Theorem 1. Additionally, the use of the long scan duration of 240 minutes leads to estimates with less overall bias because the variation in $C_S(t)/C_T(t)$ is smaller over $[100min., 240min.]$ than over the earlier window. Equivalently, as given by (14), a small variation in \bar{s} guarantees a small error in the estimated V_T . Clearly, linear methods based on the MA0 model work well during the equilibrium phase. Unfortunately, this equilibrium may be reached too late for practical application, see for example ROI 6 in Figure 5(b), for which approximate equilibrium is not reached until 3 hours. The results with 90 minutes scan duration show that better estimates are obtained for larger $(a_1 + a_2)/(b_1 - a_2)$, which consistently supports the analysis in Section 2.2.

In these simulations the accurate data and integrals are used so as to assure that the results are not impacted by use of a low accuracy numerical quadrature but instead are focused on the effects of the model error of Logan-GA and MA1. It is interesting to note, however, that the error introduced by the numerical quadrature always lowers the estimate of the V_T , see Section 5.2. Moreover, the noise from other sources may have a similar impact. This is a topic for future research.

Table 2: The V_T calculated using Logan-GA and MA1 with noise-free data and accurate integrals. V_T is calculated for scan durations $T = 90$ minutes with $t^* = 35$ minutes, and $T = 240$ minutes with $t^* = 100$ minutes. The percentage bias is listed in parentheses.

ROI ID	True V_T	35-90 min		100-240 min	
		Logan-GA	MA1	Logan-GA	MA1
1	3.9722	3.549(-10.65%)	3.542(-10.84%)	3.981(0.22%)	3.977(0.12%)
2	6.6872	6.585(-1.53%)	6.577(-1.65%)	6.709(0.33%)	6.709(0.33%)
3	4.0252	3.593(-10.73%)	3.586(-10.92%)	4.034(0.22%)	4.030(0.11%)
4	8.6706	8.342(-3.79%)	8.331(-3.92%)	8.687(0.19%)	8.685(0.16%)
5	8.5168	8.129(-4.55%)	8.117(-4.69%)	8.536(0.23%)	8.533(0.19%)
6	4.5500	3.204(-29.58%)	3.208(-29.50%)	4.281(-5.91%)	4.273(-6.10%)
7	3.2728	3.300(0.82%)	3.298(0.76%)	3.286(0.41%)	3.288(0.45%)
8	3.7480	3.635(-3.01%)	3.625(-3.28%)	3.780(0.84%)	3.779(0.84%)
9	5.9841	5.910(-1.23%)	5.902(-1.37%)	6.007(0.38%)	6.007(0.39%)
10	3.4353	3.416(-0.57%)	3.408(-0.78%)	3.462(0.77%)	3.463(0.80%)
11	3.5810	3.552(-0.81%)	3.544(-1.04%)	3.608(0.75%)	3.609(0.79%)

4.3. Algorithm Performance for Noise-Free Data

We contrast the performance of Algorithm 1 with Logan-GA, MA1 and KA for noise-free data. The use of a long scan duration (up to 90 minutes) is to assure that equilibrium is achieved as needed for GA

methods. For a method for which the bias due to model error is not impacted by the need for equilibrium, a shorter scan duration is preferred. For the results presented in Table 3 the V_T is calculated for the noise-free case over a scan duration of just 70 minutes with $t^* = 35$ minutes. Accurate integrals are used so as to focus the conclusions on the impact of the model error.

The KA solutions were obtained using two different optimization algorithms for the solution of the highly nonlinear problem, the interior point and the Marquardt-Levenberg methods, Matlab[®] functions `fmincon` and `lsqnonlin`, resp. In order to provide the most fair comparison the results presented are for `fmincon`, which gave the better solutions. The obtain reseasonable solutions we bound the 4 rate constants between $[0.1, 0.05, 0.001, 0.001]$ and $[0.5, 0.5, 0.1, 0.1]$. One may suprise why there is bias for KA with noise free data when the data are simulated with the 2T-4K model and fit with the identical model. The reason is that we can only obtain local minimum with numerical calculation. First the local minumum may not be global minimum, second, small round error may cause significant error in solution for a ill-posed inverse problem. The KA solution is very dependent on provision of a good initial value. If the initial values of k_3 and k_4 are taken very close to their true values, the estimate of the V_T may be nearly perfect. Here we use initial values for K_1, k_2, k_3 and k_4 set to $[0.2, 0.1, 0.01, 0.001]$.

For Logan-GA and MA1, solutions were also calculated for the scan duration of $T = 90$ minutes with $t^* = 35$ minutes as illustrated in Table 2. The KA results, not given, which do not require the attainment of equilibrium were comparable for both scan durations as expected. This independence with respect to the requirement of attainment of equilibrium was also observed for Algorithm 1 except for ROI **6**. In this case the neglected part in model (15) is relatively large as compared to that for the other ROIs, i.e. the ratio of $e^{-\alpha_2 t} \otimes C_P(t)$ to $e^{-\alpha_1 t} \otimes C_P(t)$ for ROI **6** is greater than that for the other ROIs. A significant reduction in the bias for ROI **6** from -12.71% (70 min.) to -7.39% (90 min.) was observed. It is clear, by comparing the results with those in Table 2, that Algorithm 1 for a scan duration of just 70 minutes is much more accurate for the calculation of the V_T than are Logan-GA and MA1 using scan durations of 90 minutes.

Table 3: V_T calculated by Logan-GA, MA1, KA and Algorithm 1 for a 70 minutes scan duration with $t^* = 35$ minutes. In each case the percentage bias is listed in parentheses.

ROI	Logan-GA	MA1	KA	Algorithm 1
1	3.395(-14.54%)	3.392(-14.61%)	3.928(-1.12%)	4.014(1.05%)
2	6.511(-2.64%)	6.506(-2.71%)	6.552(-2.02%)	6.777(1.34%)
3	3.436(-14.65%)	3.433(-14.71%)	3.982(-1.08%)	4.066(1.00%)
4	8.163(-5.86%)	8.157(-5.92%)	8.535(-1.56%)	8.743(0.83%)
5	7.931(-6.88%)	7.925(-6.95%)	8.383(-1.57%)	8.530(0.16%)
6	3.004(-33.97%)	3.007(-33.92%)	4.675(2.74%)	3.972(-12.71%)
7	3.293(0.63%)	3.292(0.58%)	3.188(-2.59%)	3.277(0.12%)
8	3.555(-5.15%)	3.549(-5.30%)	3.679(-1.84%)	3.784(0.95%)
9	5.847(-2.28%)	5.842(-2.37%)	5.859(-2.10%)	6.008(0.40%)
10	3.376(-1.73%)	3.371(-1.87%)	3.361(-2.17%)	3.451(0.47%)
11	3.506(-2.09%)	3.501(-2.24%)	3.505(-2.11%)	3.585(0.10%)

In contrasting the results with respect to only the bias in the calculation of the V_T it is clear that Algorithm 1 leads to significantly more robust solutions than Logan-GA1 and MA1 for noise-free data. On the other hand, the KA approach can lead to very good solutions, comparable and perhaps marginally better than Algorithm 1. For ROI **6**, for which the KA solution is significantly better, we recall that the solution depends on the initial values of the parameters. Changing the initial k_6 to 0.01, the resulting bias in the V_T of ROI **6** calculated by KA is increased to 31.75%. On the other hand, Algorithm 1 is not dependent on specifying initial values, and is thus more computationally robust.

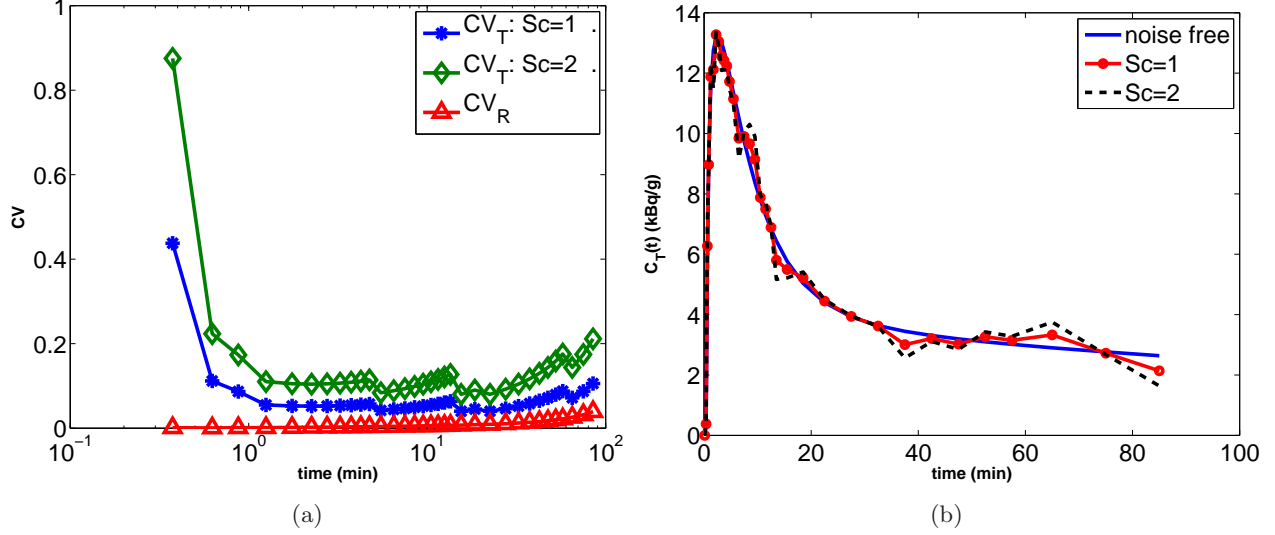


Figure 3: (a) The coefficients of variation CV_T for the noisy TTAC associated with ROI **3**, obtained with $Sc = 1$ and $Sc = 2$, resp. and CV_R , for the input function calculated for $e = 50\%$, $\mu = 0.5\text{ml}$ and $\Delta w_i = 100$ seconds. (b) The noise-free and noisy TTACs for ROI **3** obtained with $Sc = 1$ and $Sc = 2$, resp.

4.4. Experimental Design for Noisy Data

While the results with noise-free data support the use of Algorithm 1, it is more critical to assess its performance for noise-contaminated simulations. The experimental evaluation for noisy data is based on the noise-free input $u(t)$ and noise-free output $C_T(t)$, one output TTAC for each of the eleven parameter sets given in Table 1. Noise contamination of the input function and these TTACs is obtained as follows.

4.4.1. The Noise-Contaminated TTAC Data

For a given noise-free decay-corrected concentration TTAC, $C_T(t)$, Gaussian ($G(0, \sigma(C_T(t)))$) noise at each time point t_i is modeled using the approach in [8, 4, 2]. The standard deviation in the noise at each time point t_i , depends on the frame time interval Δt_i in seconds, the tracer decay constant λ (0.034 for ¹¹C) and a scale factor Sc

$$\sigma(C_T(t_i)) = Sc \sqrt{\frac{C_T(t_i) e^{\lambda t_i}}{\Delta t_i}}. \quad (18)$$

The resulting coefficients of variation CV_T (ratio $\sigma(C_T(t_i))$ to $C_T(t_i)$), for scale factors 1 and 2, are illustrated in Figure 3.

4.4.2. The Noise-Contaminated Input Function

The noise in the input function can be attributed to two sources, system and random noise. Although the random γ -ray emission follows a Poisson distribution, we use the limiting result that a large mean Poisson distribution is approximately Gaussian to model this randomness as Gaussian. Thus both sources are modeled as Gaussian but with different variance. Consider first the following model for determining the randomness of the γ -ray emissions. Suppose a μ ml blood sample is placed in a γ -ray well counter which has efficiency e and the measured counts over Δw_i seconds are $n(t_i)$. Then the measured decay corrected concentration ($\text{kBq} \cdot \text{mL}^{-1}$) is

$$C_P(t_i) = \frac{n(t_i) e^{\lambda t_i}}{1000 \Delta w_i \mu e},$$

where 1000 is a normalization factor to convert the counts to “kilo” counts. Then, assuming that the mean of $C_P(t_i)$ (or its true value) is $u(t_i)$ as given in (17), the standard deviation in the measurement of $C_P(t_i)$ due to random effects is $\sigma_R(C_P(t_i)) = \sqrt{u(t_i)e^{\lambda t_i}/(1000\Delta w_i\mu e)}$. The coefficient of variation, $CV_R = \sigma_R(C_P(t_i))/u(t_i)$, which results from this random noise is shown in Figure 3. It is assumed in the experiments that each blood sample has volume $\mu = 0.5ml$, the count duration is $\Delta w_i = 100$ seconds and the well counter efficiency is $e = 50\%$. Then, denoting the coefficient of variation due to system noise by CV_S , the noise-contaminated input is given by

$$C_P(t_i) = u(t_i)(1 + (CV_R + CV_S)\eta_i), \quad (19)$$

where η_i is selected from a standard normal distribution ($G(0, 1)$), and in the simulations we use $CV_S = 0.05$, see Figure 2.

4.5. Experimental Results for Noisy Data

Two hundred random noise realizations are generated for each input-TTAC pair, and for each noise level ($Sc = 1, 2$). The distribution volume is calculated for each experimental pair using Logan-GA, MA1, KA and Algorithm 1. In each case two scan durations are considered, 70 and 90 minutes respectively, and $t^* = 35$ minutes. Unlike the noise-free case, the numerical quadrature for $\int_0^t C_P(\tau)d\tau$ uses only the samples at scan points $C_P(t_i)$.

We present histograms for the percentage relative error of the bias $100(V_T^{\text{est}} - V_T^{\text{true}})/V_T^{\text{true}}$ in order to provide a comprehensive contrast of the methods. Table 4 numerically summarized the results and Figure 4 shows the histograms for all eleven ROIs, with the range of the error for each method indicated in the legend. The figures (a)-(b) are for scan windows of 90 minutes, for noise scale factors $Sc = 1$ and $Sc = 2$ while (c)-(d) are for scan windows of 70 minutes. It is clear that the distributions of the relative errors for KA and MA1 are far from normal; KA has a significant positive tail while Logan-GA has strong negative bias. MA1 has unacceptably long tails except for the case of low noise with long scan duration, i.e. $Sc = 1$ with 90 minutes scan duration. On the other hand, the histogram for Algorithm 1 is close to a Gaussian random distribution; the mean is near zero and the distribution is approximately symmetric. Moreover, Algorithm 1 performs well, and is only outperformed marginally by MA1 for the lower noise and longer time window case. On the other hand, there are some situations, particularly for MA1, in which the relative error is less than -100% ; in other words, the calculated V_T s are negative. Such *unsuccessful* results occur only for the higher noise level ($Sc = 2$). While there was only one such occurrence for the Logan-GA (70 min. with ROI 9), there were 40 such occurrences for MA1, 33 for the shorter time interval of 70 minutes (ROIs 1, 3, 4, 5, 6, 8 and 9) and 7 for the longer interval of 90 minutes, (ROIs 1 and 6). The reason for the negative V_T for MA1 is discussed in Section 5.4. From the results for the higher noise $Sc = 2$ we conclude that Algorithm 1 using the shorter 70 minutes scan duration outperforms the other algorithms, even in comparison to their results for the longer scan duration.

Table 4: Every case (noise levels $Sc=1$ and 2 , 11 ROIs, and scanning durations (DUR) 90 and 70 minutes) is simulated with 200 realizations. V_T s are calculated by Logan-GA, MA1, KA and Algorithm 1. Biases are listed in percentage and coefficients of variation (CV) are presented in parentheses, $\text{mean}\%(100*CV)$.

Sc	DUR	Logan-GA	MA1	KA	Alg 1
1	90	-10.95(10.61)	-6.78(10.39)	6.50(39.09)	-3.54(12.55)
	70	-15.13(12.28)	-7.62(14.64)	16.51(63.91)	-4.37(16.65)
2	90	-18.03(13.25)	16.77(732.04)	32.91(107.13)	-5.48(15.86)
	70	-25.21(15.08)	8.58(590.35)	52.95(144.11)	-11.20(18.11)

Obviously Algorithm 1 is more expensive computationally than Logan-GA and MA1. In the simulations, the average CPU time, in seconds, per TTAC was 0.00083, 0.00057, 12.2 and 0.0036, for Logan-GA,

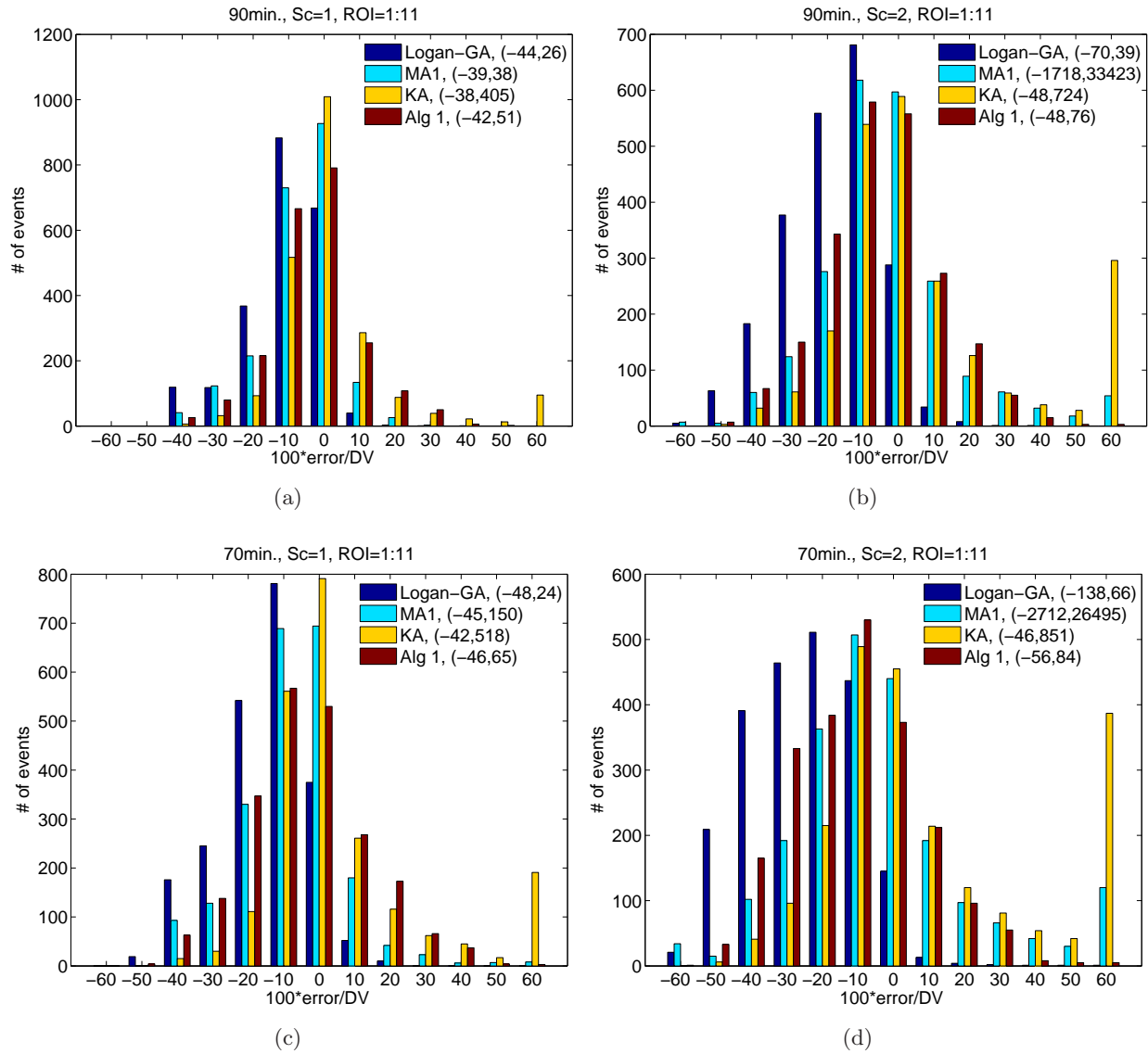


Figure 4: Histograms for normalized error (in percentage), $100(V_T^{est} - V_T^{true})/V_T^{true}$, of the results for all eleven ROIs and four methods. The error ranges are presented in the legends.

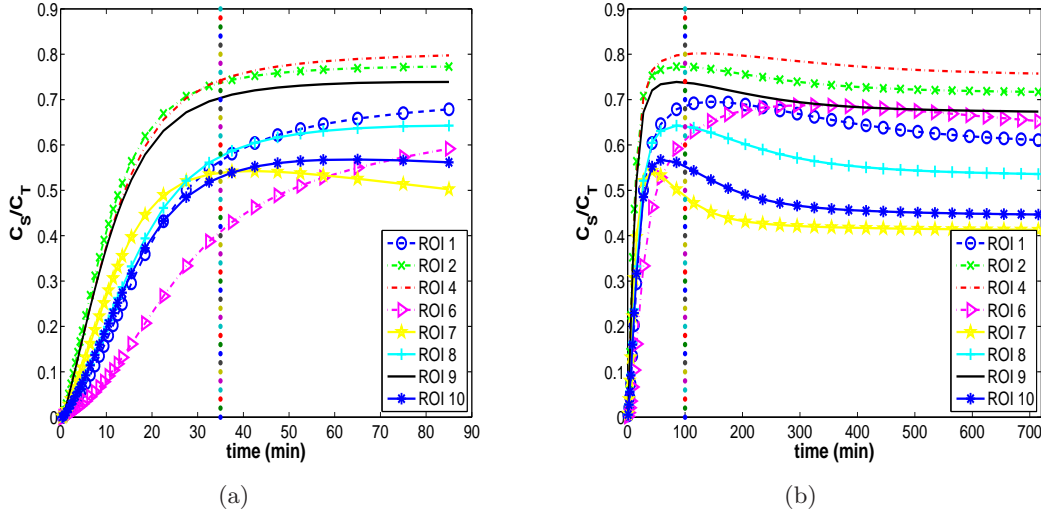


Figure 5: $C_S(t)/C_T(t)$ against time for all test ROIs except ROIs **3**, **5** and **11** for the first 90 minutes (a) and 720 minutes (b). Dotted vertical lines are plotted at time $t^* = 35$ minutes (a) and $t^* = 100$ minutes (b). The curves for ROIs **3**, **5** and **11** are similar to those for ROIs **1**, **4** and **10** resp..

MA1, KA and Algorithm 1, respectively. The high cost of the KA results from the requirement to use a nonlinear algorithm. Because the KA requires a good initial estimate for the parameters the cost is variable for each TTAC; it is dependent on whether the supplied initial value is a good initial estimate. Indeed the KA results take from 8 to 25 seconds, while the costs using the other methods are virtually TTAC independent.

5. Discussion

5.1. Equilibrium Behavior and Dependence on the Size of k_4

The graphical analysis methods of Logan-type rely on the assumption that the ratio $C_S(t)$ to $C_T(t)$ is approximately constant within a chosen window $[t^*, T]$. This ratio is plotted against time for the simulated data for ROIs **1** to **11** in Figure 5(a). **It is clear that the ratios for ROIs 1, 3 and 6 have not reached equilibrium even by 90 minutes.** These are the three data sets with the largest bias reported in Section 4.2 and with smallest k_4 (resp. k_6). It is certain that equilibrium is eventually reached. These curves first increase to a peak at about 120 minutes for ROIs **1** and **3** and at about 180 minutes for ROI **6** and then decrease before reaching approximately constant values (Figure 5(b)). On the other hand, increasing the scan duration to more than two hours is not practical. **Moreover, as illustrated in Figure 6, using the linearity of $\int_0^t C_T(\tau)d\tau/C_T(t)$ versus $\int_0^t C_T(\tau)d\tau/C_P(t)$ to verify whether equilibrium has been reached may be misleading.** For example, it would appear that all eleven data sets have achieved equilibrium after roughly 35 minutes. The arrow in Figure 6 points to the marker corresponding to the data calculated at the middle point of the frame from 35 to 40 minutes.

Errors that arise from slow binding kinetics, i.e. small k_4 is the 2-tissue compartmental model, were observed in previous literature, [3, 16]. We illustrate the relation between the bias in the estimate of V_T calculated by Logan-GA and k_4 in Figure 7. A small value of k_4 may cause a large $1/k_4$, a large variation of $C_S(t)/C_T(t)$ and consequently from (13) D can be large. The conclusion of larger D for smaller k_4 can be seen from $C_S = k_3 e^{-k_4 t} \otimes C_{ND}(t)$, which is derived from (6), and $C_S(t)/C_T(t) = C_S(t)/(C_S(t) + C_{NS+F}(t))$. it is apparent that the ratio $C_S(t)$ to $C_{ND}(t)$ is not close to a constant in finite time when k_4 is very small.

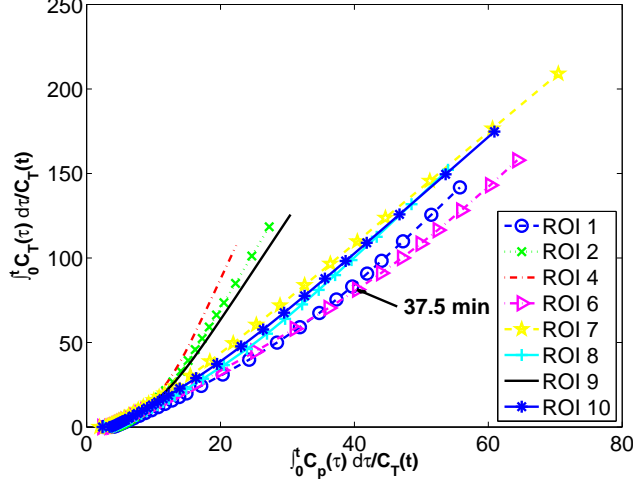


Figure 6: $\int_0^t C_T(\tau) d\tau / C_T(t)$ (y-axis) against $\int_0^t C_P(\tau) d\tau / C_T(t)$ (x-axis) for all test ROIs except ROIs **3**, **5** and **11** for the first 90 minutes. The last eight points correspond to the time interval 35 to 90 minutes. The curves for ROIs **3**, **5** and **11** are similar to those for ROIs **1**, **4** and **10** resp.. The arrow points to the first frame falling in this interval for ROI **6**.

On the other hand, when k_4 is large, $e^{-k_4 t}$ behaves like an impulse function which guarantees that $C_S(t)$ is proportional to $C_{ND}(t)$ after a very short time interval. Figure 7 verifies that **the magnitude of the bias in Logan-GA's estimation decreases as k_4 increases**, further verifying that large bias in V_T may arise purely due to modeling assumptions in the absence of noise in the data. It also confirmed the effectiveness of Algorithm 1.

5.2. The effects of quadrature error

Both Logan-GA and MA1, (2) and (3) resp., require the calculation of integrals $\int_0^t C_T(\tau) d\tau$ and $\int_0^t C_P(\tau) d\tau$. Assume the noise-free measurements $C_T(t_i)$ are derived from the integral over the i th frame duration. Thus we can easily recover its integral without introducing error. However, we can only obtain a limited number of blood samples for $C_P(t)$ in clinical practice. Thus quadrature error for calculation of $\int_0^t C_P(\tau) d\tau$ due to using a limited number of plasma samples is unavoidable. The accuracy of the numerical quadrature impacts the accuracy of the parameter estimates. Note that we classify the noise effects as another source of bias in V_T .

We recalculate the V_T for the experiments reported in Section 4.2, but now using numerical quadrature for calculation of $\int_0^t C_P(\tau) d\tau$ with data sampled one time point per time frame. The bias for each ROI of the estimated V_T using 90 minutes scan data with $t^* = 35$ minutes is -11.83% , -2.99% , -11.91% , -4.88% , -5.64% , -30.49% , -1.22% , -4.61% , -2.81% , -2.40% and -2.63% when calculated using Logan-GA, and -12.02% , -3.10% , -12.10% , -5.01% , -5.77% , -30.42% , -1.28% , -4.87% , -2.93% , -2.61% and -2.86% calculated using MA1. It is interesting to note that the V_T calculated for ROI **7** is no longer an over-estimate. This does not contradict the result of Theorem 1, which predicts that the V_T for ROI **7** will be over-estimated due to model error, provided that the other aspects of the calculation are accurate. Now using a less accurate quadrature the negative bias due to quadrature error canceled the positive bias due to the model error. Indeed, for all eleven test cases **the impact of the less accurate quadrature is to shift the bias down**, i.e. it is more negative as compared to the equivalent more accurate calculations shown in Table 2.

5.3. Bias and classification between AD and NC subjects

In the eleven simulated ROIs, large under-estimation of the V_T calculated by Logan-GA and MA1 is observed for ROIs **1** (NC Cort), **3** (NC PCG) and **6** (AD Cere). A lower value of the V_T in the cortical

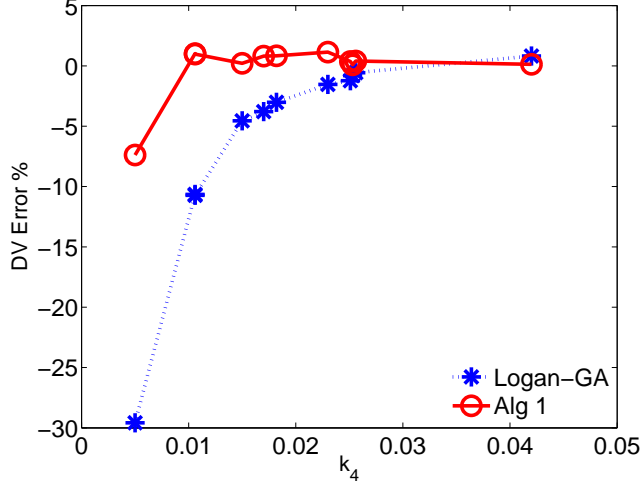


Figure 7: The bias in the Logan-GA and Algorithm 1 estimations of the V_T against the value of k_4 for the eleven ROIs, assuming noise-free data, a scan duration of 90 minutes and $t^* = 35$ minutes.

regions of NCs and in the cerebellum for AD subjects will result in under-estimation of the DVR for NCs and over-estimation of the DVR for AD subjects when the cerebellum is used as the reference region for the DVR calculation. Thus, the difference between AD and NC can be artificially enhanced, and viewed as a positive outcome associated with the bias of Logan-GA and MA1. This conclusion, however, can not be generalized. It is unknown whether it is always the case that AD/NC have small/large k_6 in cerebellar regions and relatively large/small k_4 in cortical regions. Confirmation of these assertions would suggest, based on the discussion in Sections 2.2 and 5.1, that the DVR is over-estimated for AD subjects and under-estimated for healthy subjects (also see Figure 7). In addition, more subtle differences, such as the ones between mild cognitive impairment (MCI) and NC, or among NC with differential genetic risk for AD, may make the effects of bias much less predictable. Consequently, we evaluate the quantification methods based on their bias because the goal of these methods is to estimate the V_T as accurately as possible.

5.4. When does MA1 fail?

As noted in Section 4.5, MA1 generates some results with negative V_T s. Such results are reported as *unsuccessful* in [2]. Careful study of these results shows that the negative V_T s arise when the coefficient of $\int_0^t C_T(\tau)d\tau$ in (3), $-1/b$, has the wrong sign. For most radioligand binding studies $1/b$ is a small positive number because $b > (k_3 + k_4)/(k_2k_4)$, which is usually larger than 10, see Remark (2) of Algorithm 1. Thus a small error in the estimate of $-1/b$ due to large noise in the data may change its sign. This in turn impacts the sign of the estimate of the V_T , see (3).

6. Conclusions

In this article, we quantified the model error in estimating distribution volume using graphical analysis methods. We described the conditions under which the V_T is either over- or under-estimated, and quantified the bias caused by model error. We validated our findings through simulations with noise-free data. To reduce the impact of model error, we added a simple nonlinear term to the fundamental linear model MA0, and presented a new algorithm for its solution. Simulations with noisy data demonstrate that the new algorithm is cost-effective and robust even for shorter scan durations. For PIB-PET studies, the new method using shorter scan data (70 minutes) outperforms, or is at least as good as, Logan-GA, MA1

and KA methods using longer scan data (90 minutes). The proposed approach can be easily extended for DVR estimation. This is a focus of our future work.

7. Acknowledgments

This work was supported by grants from the state of Arizona (to Drs. Guo, Reiman, Chen and Renault), the NIH (R01 AG031581, R01 MH057899 and P30 AG19610 to Dr. Reiman) and the NSF (DMS 0652833 to Dr. Renault and DMS 0513214 to Drs. Renault and Guo). The authors thank researchers from the University of Pittsburgh for their published findings, including information about PiB input function and rate constants.

A. Derivation of equation (12)

Integrating (5) and (6) from 0 to t we obtain

$$C_{ND}(t) = K_1 \int_0^t C_P(\tau) d\tau - (k_2 + k_3) \int_0^t C_{ND}(\tau) d\tau + k_4 \int_0^t C_S(\tau) d\tau, \quad (20)$$

$$C_S(t) = k_3 \int_0^t C_{ND}(\tau) d\tau - k_4 \int_0^t C_S(\tau) d\tau, \quad (21)$$

$$\begin{aligned} &= k_3 \int_0^t C_{ND}(\tau) d\tau - k_4 \int_0^t (C_T(\tau) - C_{ND}(\tau)) d\tau, \\ &= -k_4 \int_0^t C_T(\tau) d\tau + (k_3 + k_4) \int_0^t C_{ND}(\tau) d\tau. \end{aligned} \quad (22)$$

Taking the sum of equations (20) and (21) yields:

$$C_T(t) = K_1 \int_0^t C_P(\tau) d\tau - k_2 \int_0^t C_{ND}(\tau) d\tau, \quad (23)$$

and canceling $\int_0^t C_{ND}(\tau) d\tau$ from (22) using (23) gives:

$$C_S(t) = -k_4 \int_0^t C_T(\tau) d\tau + \frac{k_3 + k_4}{k_2} \left(K_1 \int_0^t C_P(\tau) d\tau - C_T(t) \right).$$

This can be transformed to (12) immediately by using $V_T = \frac{K_1}{k_2} (1 + \frac{k_3}{k_4})$.

B. Fundamental theory for Corollary 1

Here we present the theoretical result from which Theorem 1 is obtained. We use the notation that $\mathbf{a} = (a_1, a_2, \dots, a_n)^T$ and $\mathbf{b} = (b_1, b_2, \dots, b_n)^T$, are vectors with entries a_i and b_i , resp. The notation \mathbf{a}/\mathbf{b} and $\mathbf{a} \circ \mathbf{b}$ denotes component wise division and multiplication, namely entries a_i/b_i and $a_i b_i$, $\|\mathbf{a}\|_1$ is $\sum_{i=1}^n |a_i|$ and $\|\mathbf{a}\|_2 = \sqrt{a_1^2 + a_2^2 + \dots + a_n^2}$ is the Euclidean norm. We call \mathbf{a} decreasing (**increasing**) if $a_1 \geq a_2 \geq \dots \geq a_n$ ($\mathbf{a}_1 \leq \mathbf{a}_2 \leq \dots \leq \mathbf{a}_n$), and non-constant decreasing (**non-constant increasing**) if it is decreasing (**increasing**) and at least one of the \geq (\leq) signs is strict, $>$ ($<$). If all of the \geq (\leq) signs are strict, we call \mathbf{a} strictly decreasing (**strictly increasing**). A vector \mathbf{a} is constant if $a_i = a$ for some constant a and for all i .

Lemma 1. (Chebyshev's sum inequality [21]) *Given real numbers $a_1 \geq a_2 \geq \dots \geq a_n$ and $b_1 \geq b_2 \geq \dots \geq b_n$, then*

$$\frac{1}{n} \sum_{k=1}^n a_k b_k \geq \left(\frac{1}{n} \sum_{k=1}^n a_k \right) \left(\frac{1}{n} \sum_{k=1}^n b_k \right). \quad (24)$$

Similarly, if $a_1 \geq a_2 \geq \dots \geq a_n$ and $b_1 \leq b_2 \leq \dots \leq b_n$, then

$$\frac{1}{n} \sum_{k=1}^n a_k b_k \leq \left(\frac{1}{n} \sum_{k=1}^n a_k \right) \left(\frac{1}{n} \sum_{k=1}^n b_k \right). \quad (25)$$

In the above Chebyshev's sum inequalities the numbers are not required to be positive and the equality is true if and only if one of the two vectors, \mathbf{a} or \mathbf{b} , is a constant vector. If \mathbf{a} and \mathbf{b} are positive vectors, the Chebyshev's sum inequalities can be expressed as $\mathbf{a}^T \mathbf{b} \geq \frac{1}{n} \|\mathbf{a}\|_1 \|\mathbf{b}\|_1$ and $\mathbf{a}^T \mathbf{b} \leq \frac{1}{n} \|\mathbf{a}\|_1 \|\mathbf{b}\|_1$.

Lemma 2. *If \mathbf{p} , \mathbf{q} and \mathbf{s} are positive real vectors, of which \mathbf{p} is a increasing vector and \mathbf{q} is a decreasing vector, then*

1. $\|\mathbf{q}\|_2^2 \mathbf{p}^T \mathbf{s} - \mathbf{p}^T \mathbf{q} \mathbf{q}^T \mathbf{s} \geq 0$ *if \mathbf{s}/\mathbf{q} is a non-constant increasing vector. The inequality is strict if \mathbf{p} is strictly increasing.*
2. $\|\mathbf{q}\|_2^2 \mathbf{p}^T \mathbf{s} - \mathbf{p}^T \mathbf{q} \mathbf{q}^T \mathbf{s} \leq 0$ *if \mathbf{s}/\mathbf{q} is a non-constant decreasing vector. The inequality is strict if \mathbf{p} is strictly increasing.*
3. $\|\mathbf{q}\|_2^2 \mathbf{p}^T \mathbf{s} - \mathbf{p}^T \mathbf{q} \mathbf{q}^T \mathbf{s} = 0$ *if \mathbf{s}/\mathbf{q} is a constant vector,*
4. $\|\mathbf{p}\|_2^2 \mathbf{q}^T \mathbf{s} - \mathbf{p}^T \mathbf{q} \mathbf{p}^T \mathbf{s} \geq 0$ *if \mathbf{s}/\mathbf{p} is a non-constant decreasing vector. The inequality is strict if \mathbf{p} is strictly increasing.*
5. $\|\mathbf{p}\|_2^2 \mathbf{q}^T \mathbf{s} - \mathbf{p}^T \mathbf{q} \mathbf{p}^T \mathbf{s} \leq 0$ *if \mathbf{s}/\mathbf{p} is a non-constant increasing vector. The inequality is strict if \mathbf{p} is strictly increasing.*
6. $\|\mathbf{p}\|_2^2 \mathbf{q}^T \mathbf{s} - \mathbf{p}^T \mathbf{q} \mathbf{p}^T \mathbf{s} = 0$ *if \mathbf{s}/\mathbf{p} is a constant vector.*

Proof. We only prove the first case. The proof for the other items follows similarly. We use mathematical induction. For the lowest dimension $n = 2$,

$$\begin{aligned} & \|\mathbf{q}\|_2^2 \mathbf{p}^T \mathbf{s} - \mathbf{p}^T \mathbf{q} \mathbf{q}^T \mathbf{s} \\ &= (q_1^2 + q_2^2)(p_1 s_1 + p_2 s_2) - (p_1 q_1 + p_2 q_2)(q_1 s_1 + q_2 s_2) \\ &= q_1^2 p_2 s_2 + q_2^2 p_1 s_1 - p_1 q_1 q_2 s_2 - p_2 q_2 q_1 s_1 \\ &= (q_1 s_2 - q_2 s_1)(q_1 p_2 - q_2 p_1) \\ &= (q_1 p_2 - q_2 p_1) \left((q_1 q_2) \left(\frac{s_2}{q_2} - \frac{s_1}{q_1} \right) \right) \\ &\geq 0. \end{aligned}$$

The last reduction follows from the monotonicity of \mathbf{p} , \mathbf{q} , which implies $q_1 p_2 - q_2 p_1 \geq 0$, and the non-constant increasing assumption of \mathbf{s}/\mathbf{q} , which guarantees $\frac{s_2}{q_2} - \frac{s_1}{q_1} > 0$. When \mathbf{p} is strictly increasing $q_1 p_2 - q_2 p_1 > 0$. Under this condition $\|\mathbf{q}\|_2^2 \mathbf{p}^T \mathbf{s} - \mathbf{p}^T \mathbf{q} \mathbf{q}^T \mathbf{s} > 0$ for $n = 2$. Assuming the inequality $\|\mathbf{q}\|_2^2 \mathbf{p}^T \mathbf{s} - \mathbf{p}^T \mathbf{q} \mathbf{q}^T \mathbf{s} \geq 0$ is true for dimension $n = i$, i.e.

$$\sum_{k=1}^i q_k^2 \sum_{k=1}^i p_k s_k - \sum_{k=1}^i p_k q_k \sum_{k=1}^i q_k s_k \geq 0,$$

then for $n = i + 1$

$$\begin{aligned}
& \|\mathbf{q}\|_2^2 \mathbf{p}^T \mathbf{s} - \mathbf{p}^T \mathbf{q} \mathbf{q}^T \mathbf{s} \\
&= \left(\sum_{k=1}^i q_k^2 + q_{i+1}^2 \right) \left(\sum_{k=1}^i p_k s_k + p_{i+1} s_{i+1} \right) - \left(\sum_{k=1}^i p_k q_k + p_{i+1} q_{i+1} \right) \left(\sum_{k=1}^i q_k s_k + q_{i+1} s_{i+1} \right) \\
&= \left(\sum_{k=1}^i q_k^2 \sum_{k=1}^i p_k s_k - \sum_{k=1}^i p_k q_k \sum_{k=1}^i q_k s_k \right) \\
&\quad + \left(p_{i+1} s_{i+1} \sum_{k=1}^i q_k^2 - q_{i+1} s_{i+1} \sum_{k=1}^i p_k q_k \right) + \left(q_{i+1}^2 \sum_{k=1}^i p_k s_k - p_{i+1} q_{i+1} \sum_{k=1}^i q_k s_k \right) \\
&\geq 0 + s_{i+1} \sum_{k=1}^i q_k (q_k p_{i+1} - p_k q_{i+1}) + q_{i+1} \sum_{k=1}^i s_k (q_{i+1} p_k - p_{i+1} q_k) \\
&= \sum_{k=1}^i (q_k p_{i+1} - p_k q_{i+1}) (q_k s_{i+1} - q_{i+1} s_k) \\
&= \sum_{k=1}^i \left((q_k p_{i+1} - p_k q_{i+1}) (q_k q_{i+1}) \right) \left(\frac{s_{i+1}}{q_{i+1}} - \frac{s_k}{q_k} \right). \\
&\geq 0.
\end{aligned}$$

The last reduction is based on the monotonicity of \mathbf{p}, \mathbf{q} and \mathbf{s}/\mathbf{q} . When \mathbf{p} is strictly increasing $q_k p_{i+1} - p_k q_{i+1} > 0$ for all $k \leq i$ the inequality will be strict because at least one of the terms $\frac{s_{i+1}}{q_{i+1}} - \frac{s_k}{q_k}$, $k = 1, \dots, i$, is positive based on the monotonicity condition. The result thus follows by induction for all integers $n \geq 2$. \square

The following corollary now follows immediately by observing that \mathbf{s}/\mathbf{q} increases when \mathbf{s} increases and \mathbf{s}/\mathbf{p} decreases when \mathbf{s} decreases.

Corollary 1. *If \mathbf{p}, \mathbf{q} and \mathbf{s} are positive real vectors, of which \mathbf{p} is a strictly increasing vector and \mathbf{q} is a decreasing vector, then*

1. $\|\mathbf{p}\|_2^2 \mathbf{q}^T \mathbf{s} - \mathbf{p}^T \mathbf{q} \mathbf{p}^T \mathbf{s} > 0$ if \mathbf{s} is a decreasing vector.
2. $\|\mathbf{q}\|_2^2 \mathbf{p}^T \mathbf{s} - \mathbf{p}^T \mathbf{q} \mathbf{q}^T \mathbf{s} > 0$ if \mathbf{s} is an increasing vector.

Lemma 3. *If $\mathbf{p}, \mathbf{q}, \mathbf{r}$ and \mathbf{s} are positive real vectors, of which \mathbf{p} is strictly increasing, \mathbf{q} is decreasing, and $\mathbf{p}, \mathbf{r}, \mathbf{s}$ and x^* satisfy $\mathbf{p}x^* - \mathbf{s} = \mathbf{r}$; and $[\hat{x}, \hat{b}] = \operatorname{argmin} \|\mathbf{p}x - \mathbf{b}q - \mathbf{r}\|_2^2$; then*

1. the estimated solution \hat{x} and exact solution x^* are related by
 - $\hat{x} > x^*$ if \mathbf{s}/\mathbf{q} is a non-constant decreasing vector,
 - $\hat{x} < x^*$ if \mathbf{s}/\mathbf{q} is a non-constant increasing vector,
 - $\hat{x} = x^*$ if \mathbf{s}/\mathbf{q} is a constant vector;
2. the following inequality is true without any monotonicity assumptions:

$$|\hat{x} - x^*| \leq \frac{\mathbf{p}^T \mathbf{q} \|\mathbf{q}\|_2^2}{\|\mathbf{p}\|_2^2 \|\mathbf{q}\|_2^2 - (\mathbf{p}^T \mathbf{q})^2} V(\bar{\mathbf{s}}), \quad (26)$$

where $\bar{\mathbf{s}} = \mathbf{s}/\mathbf{q}$ and $V(\mathbf{x}) = |\max(\mathbf{x}) - \min(\mathbf{x})|$.

3. the sign of the intercept \hat{b} is determined as follows:

- $\hat{b} > 0$ if \mathbf{s}/\mathbf{p} is a non-constant decreasing vector,
- $\hat{b} < 0$ if \mathbf{s}/\mathbf{p} is a non-constant increasing vector,
- $\hat{b} = 0$ if \mathbf{s}/\mathbf{p} is a constant vector;

4. given $x = x^*$, the LS solution of $\mathbf{p}x - \mathbf{b}\mathbf{q} \approx \mathbf{r}$ for b is $b = \mathbf{q}^T \mathbf{s} / \|\mathbf{q}\|_2^2$;
5. given $b = \mathbf{q}^T \mathbf{s} / \|\mathbf{q}\|_2^2$, the LS solution of $\mathbf{p}x - \mathbf{b}\mathbf{q} \approx \mathbf{r}$ for x and the true solution x^* have the same relationship as stated in the first conclusion of this theorem.

Proof. It is easy to verify that the LS solution of $\mathbf{p}x - \mathbf{b}\mathbf{q} \approx \mathbf{r}$ is

$$\hat{x} = \frac{\|\mathbf{q}\|_2^2 \mathbf{p}^T \mathbf{r} - \mathbf{p}^T \mathbf{q} \mathbf{q}^T \mathbf{r}}{\|\mathbf{p}\|_2^2 \|\mathbf{q}\|_2^2 - (\mathbf{p}^T \mathbf{q})^2}, \quad \hat{b} = \frac{-\|\mathbf{p}\|_2^2 \mathbf{q}^T \mathbf{r} + \mathbf{p}^T \mathbf{q} \mathbf{p}^T \mathbf{r}}{\|\mathbf{p}\|_2^2 \|\mathbf{q}\|_2^2 - (\mathbf{p}^T \mathbf{q})^2}.$$

The proof then follows as outlined below:

1. Replace \mathbf{r} in the expression for \hat{x} with $\mathbf{p}x^* - \mathbf{s}$. Then

$$\begin{aligned} \hat{x} &= \frac{\|\mathbf{q}\|_2^2 \mathbf{p}^T (\mathbf{p}x^* - \mathbf{s}) - \mathbf{p}^T \mathbf{q} \mathbf{q}^T (\mathbf{p}x^* - \mathbf{s})}{\|\mathbf{p}\|_2^2 \|\mathbf{q}\|_2^2 - (\mathbf{p}^T \mathbf{q})^2} \\ &= x^* + \frac{\mathbf{p}^T \mathbf{q} \mathbf{q}^T \mathbf{s} - \|\mathbf{q}\|_2^2 \mathbf{p}^T \mathbf{s}}{\|\mathbf{p}\|_2^2 \|\mathbf{q}\|_2^2 - (\mathbf{p}^T \mathbf{q})^2}, \end{aligned} \quad (27)$$

and the results immediately follow from Lemma 2 (1)-(3) and the fact $\|\mathbf{p}\|_2 \|\mathbf{q}\|_2 > \mathbf{p}^T \mathbf{q}$ when \mathbf{p} is not linear proportional to \mathbf{q} .

2. Because

$$\begin{aligned} &\mathbf{p}^T \mathbf{q} \mathbf{q}^T \mathbf{s} - \|\mathbf{q}\|_2^2 \mathbf{p}^T \mathbf{s} \\ &= \mathbf{p}^T \mathbf{q} (\mathbf{q} \circ \mathbf{q})^T \bar{\mathbf{s}} - \|\mathbf{q}\|_2^2 (\mathbf{p} \circ \mathbf{q})^T \bar{\mathbf{s}} \\ &\leq \mathbf{p}^T \mathbf{q} \|\mathbf{q}\|_2^2 \max_i(\bar{s}_i) - \|\mathbf{q}\|_2^2 \mathbf{p}^T \mathbf{q} \cdot \min_i(\bar{s}_i) \\ &= \mathbf{p}^T \mathbf{q} \|\mathbf{q}\|_2^2 (\max_i(\bar{s}_i) - \min_i(\bar{s}_i)), \end{aligned}$$

and similarly

$$\mathbf{p}^T \mathbf{q} \mathbf{q}^T \mathbf{s} - \|\mathbf{q}\|_2^2 \mathbf{p}^T \mathbf{s} \geq \mathbf{p}^T \mathbf{q} \|\mathbf{q}\|_2^2 (\min_i(\bar{s}_i) - \max_i(\bar{s}_i)),$$

We have

$$|\mathbf{p}^T \mathbf{q} \mathbf{q}^T \mathbf{s} - \|\mathbf{q}\|_2^2 \mathbf{p}^T \mathbf{s}| \leq \mathbf{p}^T \mathbf{q} \|\mathbf{q}\|_2^2 (\min_i(\bar{s}_i) - \max_i(\bar{s}_i)).$$

Using the fact $\|\mathbf{p}\|_2^2 \|\mathbf{q}\|_2^2 - (\mathbf{p}^T \mathbf{q})^2 > 0$ and (27), we conclude the inequality is true.

3. Again we replace \mathbf{r} with $\mathbf{p}x^* - \mathbf{s}$, then the expression for \hat{b} becomes

$$\begin{aligned} \hat{b} &= \frac{-\|\mathbf{p}\|_2^2 \mathbf{q}^T (\mathbf{p}x^* - \mathbf{s}) + \mathbf{p}^T \mathbf{q} \mathbf{p}^T (\mathbf{p}x^* - \mathbf{s})}{\|\mathbf{p}\|_2^2 \|\mathbf{q}\|_2^2 - (\mathbf{p}^T \mathbf{q})^2} \\ &= \frac{\|\mathbf{p}\|_2^2 \mathbf{q}^T \mathbf{s} - \mathbf{p}^T \mathbf{q} \mathbf{p}^T \mathbf{s}}{\|\mathbf{p}\|_2^2 \|\mathbf{q}\|_2^2 - (\mathbf{p}^T \mathbf{q})^2}. \end{aligned} \quad (28)$$

The results immediately follow from Lemma 2 (4)-(6) and the fact $\|\mathbf{p}\|_2 \|\mathbf{q}\|_2 > \mathbf{p}^T \mathbf{q}$ when \mathbf{p} and \mathbf{q} do not have the same direction.

4. This result is easily verified.

5. Given $b = \mathbf{q}^T \mathbf{s} / \|\mathbf{q}\|_2^2$, the LS solution of $\mathbf{p}x - b\mathbf{q} \approx \mathbf{r}$ for x is

$$\begin{aligned}\hat{x} &= \frac{1}{\|\mathbf{p}\|_2^2} \mathbf{p}^T (\mathbf{q}b + \mathbf{r}) \\ &= \frac{1}{\|\mathbf{p}\|_2^2} (\mathbf{p}^T \mathbf{q} \frac{\mathbf{q}^T \mathbf{s}}{\|\mathbf{q}\|_2^2} + \mathbf{p}^T (\mathbf{p}x^* - \mathbf{s})) \\ &= x^* + \frac{\mathbf{p}^T \mathbf{q} \mathbf{q}^T \mathbf{s} - \|\mathbf{q}\|_2^2 \mathbf{p}^T \mathbf{s}}{\|\mathbf{p}\|_2^2 \|\mathbf{q}\|_2^2}.\end{aligned}$$

The results now follow from Lemma 2. □

We now transform the exact equation to $\mathbf{p}/\mathbf{q}x^* - \mathbf{s}/\mathbf{q} = \mathbf{r}/\mathbf{q}$ and rewrite the results using vectors $\bar{\mathbf{p}} = \mathbf{p}/\mathbf{q}$, $\bar{\mathbf{s}} = \mathbf{s}/\mathbf{q}$ and $\bar{\mathbf{r}} = \mathbf{r}/\mathbf{q}$. Correspondingly, we find the LS solution of $\bar{\mathbf{p}}x - \mathbf{e}b \approx \bar{\mathbf{r}}$ for $\mathbf{e} = (1, 1, \dots, 1)^T$.

Corollary 2. *If $\bar{\mathbf{p}}$, $\bar{\mathbf{r}}$ and $\bar{\mathbf{s}}$ are positive, of which $\bar{\mathbf{p}}$ is strictly increasing, $\bar{\mathbf{p}}$, $\bar{\mathbf{r}}$, $\bar{\mathbf{s}}$ and x^* satisfy $\bar{\mathbf{p}}x^* - \bar{\mathbf{s}} = \bar{\mathbf{r}}$; and $[\hat{x}, \hat{b}] = \operatorname{argmin} \|\bar{\mathbf{p}}x - \mathbf{e}b - \bar{\mathbf{r}}\|_2^2$, then*

1. *the estimated solution \hat{x} and the exact solution x^* are related by*

- $\hat{x} > x^*$ if $\bar{\mathbf{s}}$ is a non-constant decreasing vector,
- $\hat{x} < x^*$ if $\bar{\mathbf{s}}$ is a non-constant increasing vector,
- $\hat{x} = x^*$ if $\bar{\mathbf{s}}$ is a constant vector;

Moreover, the following inequality is true without any monotonicity assumptions.

$$|\hat{x} - x^*| \leq \frac{n \|\bar{\mathbf{p}}\|_1}{n \|\bar{\mathbf{p}}\|_2^2 - \|\bar{\mathbf{p}}\|_1^2} V(\bar{\mathbf{s}}). \quad (29)$$

2. *The sign of the intercept \hat{b} is determined as follows:*

- $\hat{b} > 0$ if $\bar{\mathbf{s}}/\bar{\mathbf{p}}$ is a non-constant decreasing vector,
- $\hat{b} < 0$ if $\bar{\mathbf{s}}/\bar{\mathbf{p}}$ is a non-constant increasing vector,
- $\hat{b} = 0$ if $\bar{\mathbf{s}}/\bar{\mathbf{p}}$ is a constant vector.

In addition,

- $\hat{b} > \sum_{i=1}^n \bar{s}_i/n$ if $\bar{\mathbf{s}}$ is a non-constant decreasing vector,
- $\hat{b} < \sum_{i=1}^n \bar{s}_i/n$ if $\bar{\mathbf{s}}$ is a non-constant increasing vector,
- $\hat{b} = \sum_{i=1}^n \bar{s}_i/n$ if $\bar{\mathbf{s}}$ is a constant vector;

3. *Given $x = x^*$, the LS solution of $\bar{\mathbf{p}}x - \mathbf{e}b \approx \bar{\mathbf{r}}$ for b is $b = \sum_{i=1}^n \bar{s}_i/n$;*

4. *Given $b = \sum_{i=1}^n \bar{s}_i/n$, the LS solution of $\bar{\mathbf{p}}x - \mathbf{e}b \approx \bar{\mathbf{r}}$ for x and the true solution x^* are related as stated in the first conclusion of this theorem.*

Proof. Most results are a direct Corollary of Lemma 3 by setting $\mathbf{q} = \mathbf{e}$. We only prove the new results (1) and (2).

1. We just need to prove the bounds for $|\hat{x} - x^*|$. Setting $\mathbf{q} = \mathbf{e}$ in (27) we have

$$\hat{x} = x^* + \frac{\|\bar{\mathbf{p}}\|_1 \sum_i \bar{s}_i - n\bar{\mathbf{p}}^T \bar{\mathbf{s}}}{n\|\bar{\mathbf{p}}\|_2^2 - \|\bar{\mathbf{p}}\|_1^2}. \quad (30)$$

Because

$$\|\bar{\mathbf{p}}\|_1 \sum_i \bar{s}_i - n\bar{\mathbf{p}}^T \bar{\mathbf{s}} \leq n \cdot \max_i(\bar{s}_i) \|\bar{\mathbf{p}}\|_1 - n \cdot \min_i(\bar{s}_i) \|\bar{\mathbf{p}}\|_1 = n\|\bar{\mathbf{p}}\|_1 (\max_i(\bar{s}_i) - \min_i(\bar{s}_i)),$$

$$\|\bar{\mathbf{p}}\|_1 \sum_i \bar{s}_i - n\bar{\mathbf{p}}^T \bar{\mathbf{s}} \geq n \cdot \min_i(\bar{s}_i) \|\bar{\mathbf{p}}\|_1 - n \cdot \max_i(\bar{s}_i) \|\bar{\mathbf{p}}\|_1 = n\|\bar{\mathbf{p}}\|_1 (\min_i(\bar{s}_i) - \max_i(\bar{s}_i)),$$

and $n\|\bar{\mathbf{p}}\|_2^2 - \|\bar{\mathbf{p}}\|_1^2 > 0$ we obtain

$$\begin{aligned} |\hat{x} - x^*| &= \frac{\|\bar{\mathbf{p}}\|_1 \sum_i \bar{s}_i - n\bar{\mathbf{p}}^T \bar{\mathbf{s}}}{n\|\bar{\mathbf{p}}\|_2^2 - \|\bar{\mathbf{p}}\|_1^2} \\ &\leq \frac{n\|\bar{\mathbf{p}}\|_1 (\max_i(\bar{s}_i) - \min_i(\bar{s}_i))}{n\|\bar{\mathbf{p}}\|_2^2 - \|\bar{\mathbf{p}}\|_1^2} \\ &= \frac{n\|\bar{\mathbf{p}}\|_1}{n\|\bar{\mathbf{p}}\|_2^2 - \|\bar{\mathbf{p}}\|_1^2} V(\bar{\mathbf{s}}). \end{aligned}$$

2. Setting $\mathbf{q} = \mathbf{e}$ in (28) we have

$$\hat{b} = \frac{\|\bar{\mathbf{p}}\|_2^2 \|\bar{\mathbf{s}}\|_1 - \|\bar{\mathbf{p}}\|_1 \bar{\mathbf{p}}^T \bar{\mathbf{s}}}{n\|\bar{\mathbf{p}}\|_2^2 - \|\bar{\mathbf{p}}\|_1^2}.$$

The results on the sign follow from Lemma 3 (3). For the remaining three inequalities, we only prove the case for which $\bar{\mathbf{s}}$ is decreasing. Proofs of the other two are similar. Setting $\mathbf{q} = \mathbf{e}$ in (28) we have

$$\begin{aligned} \hat{b} &= \frac{\|\bar{\mathbf{p}}\|_2^2 \|\bar{\mathbf{s}}\|_1 - \|\bar{\mathbf{p}}\|_1 \bar{\mathbf{p}}^T \bar{\mathbf{s}}}{n\|\bar{\mathbf{p}}\|_2^2 - \|\bar{\mathbf{p}}\|_1^2} \\ &> \frac{\|\bar{\mathbf{p}}\|_2^2 \|\bar{\mathbf{s}}\|_1 - \|\bar{\mathbf{p}}\|_1 \frac{1}{n} \|\bar{\mathbf{p}}\|_1 \|\bar{\mathbf{s}}\|_1}{n\|\bar{\mathbf{p}}\|_2^2 - \|\bar{\mathbf{p}}\|_1^2} \\ &= \frac{\|\bar{\mathbf{s}}\|_1}{n} = \frac{\sum_{i=1}^n \bar{s}_i}{n}. \end{aligned}$$

□

C. Robust analysis for LS solution of (16)

In Remark 2, we claimed that “the estimate of V_T is much more robust to noise in the formulation than are the estimates of A and B because $\int_0^t C_P(\tau) d\tau$ is much larger than both $C_T(t)$ and $C_S(t)$ for $t > t^*$ ”. Here we present a theoretical explanation, which is helpful for algorithm design in quantification. Instead of considering a general linear equation, which is out of the range of this paper, we assume a system of equations $\mathbf{A}\mathbf{x} = \mathbf{y}$ with only two independent variables $\mathbf{x} = [x_1, x_2]^T$. The two columns of the system matrix A are denoted by \mathbf{a}_1 and \mathbf{a}_2 , i.e. $A = [\mathbf{a}_1, \mathbf{a}_2]$.

Theorem 2. Suppose the linear system $\mathbf{A}\mathbf{x} \approx \mathbf{y} + \epsilon$, for $\mathbf{A} = [\mathbf{a}_1, \mathbf{a}_2]$, has the exact solution $\mathbf{x} = [x_1^*, x_2^*]$, the uncorrelated noise vector ϵ obeys a multi-variable Gaussian distribution with zero means and common variance σ^2 and that $\|\mathbf{a}_1\| \gg \|\mathbf{a}_2\|$. Then least squares solution $\hat{\mathbf{x}} = [\hat{x}_1, \hat{x}_2]^T$ has the following statistical properties

1. $E(\hat{x}_1) = x_1^*$ and $E(\hat{x}_2) = x_2^*$, and
2. $\text{Var}(\hat{x}_1) \ll \text{Var}(\hat{x}_2)$.

Proof. We assume matrix \mathbf{A} has the following singular value decomposition

$$\mathbf{A} = [\mathbf{a}_1, \mathbf{a}_2] = \mathbf{U}\mathbf{S}\mathbf{V}^T = \mathbf{U} \begin{pmatrix} s_1 & 0 \\ 0 & s_2 \\ \vdots & \dots \\ 0 & 0 \end{pmatrix} \begin{pmatrix} \cos \theta & \sin \theta \\ -\sin \theta & \cos \theta \end{pmatrix}, \quad (31)$$

in which $s_1 \geq s_2$. Then

$$\hat{\mathbf{x}} = \mathbf{V}\mathbf{S}^\dagger\mathbf{U}^T(\mathbf{y} + \epsilon) = \mathbf{x}^* + \mathbf{V}\mathbf{S}^\dagger\mathbf{U}^T\epsilon,$$

where

$$\mathbf{S}^\dagger = \begin{pmatrix} 1/s_1 & 0 & \dots & 0 \\ 0 & 1/s_2 & \dots & 0 \end{pmatrix}.$$

Because \mathbf{U} is an unitary matrix and $\|\mathbf{a}_1\| \gg \|\mathbf{a}_2\|$ we immediately derive the the following inequality from equation (31):

$$s_1^2 \cos^2 \theta + s_2^2 \sin^2 \theta \gg s_1^2 \sin^2 \theta + s_2^2 \cos^2 \theta.$$

This inequality is equivalent to $(s_1^2 - s_2^2) \cos^2 \theta + s_2^2 \gg (s_1^2 - s_2^2) \sin^2 \theta + s_2^2$, which implies $\cos^2 \theta \gg \sin^2 \theta$, i.e. $\cos^2 \theta \approx 1$ and $\sin^2 \theta \approx 0$, and $s_1^2 \gg s_2^2$. If we denote the two rows of matrix $\mathbf{V}\mathbf{S}^\dagger$ by \mathbf{q}_1 and \mathbf{q}_2 then

$$\begin{aligned} \|\mathbf{q}_1\|^2 &= \sin^2 \theta / s_1^2 + \cos^2 \theta / s_2^2 = 1/s_1^2 + \cos^2 \theta (1/s_2^2 - 1/s_1^2), \\ \|\mathbf{q}_2\|^2 &= \cos^2 \theta / s_1^2 + \sin^2 \theta / s_2^2 = 1/s_1^2 + \sin^2 \theta (1/s_2^2 - 1/s_1^2). \end{aligned}$$

Because $\cos^2 \theta \gg \sin^2 \theta$ and $1/s_2^2 \gg 1/s_1^2$ we conclude $\|\mathbf{q}_2\|^2 \gg \|\mathbf{q}_1\|^2$. If we let \mathbf{p}_1 and \mathbf{p}_2 be the two rows of matrix $\mathbf{V}\mathbf{S}^\dagger\mathbf{U}^T$ then $\|\mathbf{p}_1\| = \|\mathbf{q}_1\|$ and $\|\mathbf{p}_2\| = \|\mathbf{q}_2\|$ because \mathbf{U} is unitary. Thus $\|\mathbf{p}_2\|^2 \gg \|\mathbf{p}_1\|^2$. Let

$$\mathbf{d} = \hat{\mathbf{x}} - \mathbf{x}^* = \mathbf{V}\mathbf{S}^\dagger\mathbf{U}^T\epsilon.$$

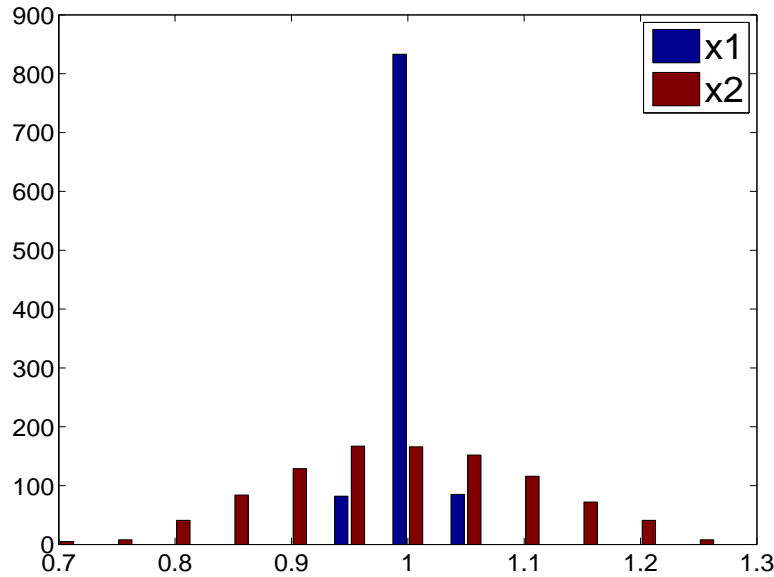
It is clear $E(d_1) = 0$ and $E(d_2) = 0$ because the means of ϵ are zero, and $\text{Var}(d_1) = \sum_i p_{1i}^2 \sigma^2 = \|\mathbf{p}_1\|^2 \sigma^2$ and $\text{Var}(d_2) = \sum_i p_{2i}^2 \sigma^2 = \|\mathbf{p}_2\|^2 \sigma^2$ resp.. Therefore $\text{Var}(\hat{d}_1) \ll \text{Var}(\hat{d}_2)$. Because $\mathbf{d} = \hat{\mathbf{x}} - \mathbf{x}^*$ we conclude $E(\hat{\mathbf{x}}) = \mathbf{x}^*$ and $\text{Var}(\hat{x}_1) \ll \text{Var}(\hat{x}_2)$ \square

This result is illustrated by the following simple example:

$$\begin{pmatrix} 4 & 1 \\ 8 & 1 \\ 10 & 1 \end{pmatrix} \mathbf{x} = \begin{pmatrix} 5 \\ 9 \\ 11 \end{pmatrix} + \begin{pmatrix} \epsilon_1 \\ \epsilon_2 \\ \epsilon_3 \end{pmatrix}$$

The first column is much larger than the second column and the exact solution is $\mathbf{x} = [x_1, x_2] = [1, 1]$. If we add 1% noise to the right hand side, i.e. $\epsilon_1 \sim N(0, 0.05)$, $\epsilon_2 \sim N(0, 0.09)$ and $\epsilon_3 \sim N(0, 0.115)$, and perform simulation with 1000 realizations the distribution of the resulting x_1 and x_2 are illustrated in Figure 8. These results are consistent with the conclusions in Theorem 2. We see that the unknown associated with the larger column, x_1 , is more robust to noise than the other one, x_2 .

Figure 8: LS solution histograms for x_1 and x_2 . 1000 realizations with 1% noise in data are performed.



References

- [1] M. Slifstein, M. Laruelle, Effects of statistical noise on graphic analysis of PET neuroreceptor studies, *J. Nucl. Med.* 41 (12) (2000) 2083–8.
- [2] M. Ichise, H. Toyama, R. Innis, R. Carson, Strategies to improve neuroreceptor parameter estimation by linear regression analysis., *J. Cereb. Blood Flow Metab.* 22 (10) (2002) 1271–81.
- [3] J. Logan, A review of graphical methods for tracer studies and strategies to reduce bias, *Nuclear Medicine and Biology* 30 (8) (2003) 833–844.
- [4] J. Varga, Z. Szabo, Modified regression model for the Logan plot, *J. Cereb. Blood Flow Metab.* 22 (2) (2002) 240–4.
- [5] R. Ogden, Estimation of kinetic parameters in graphical analysis of PET imaging data, *Stat. Med.* 22 (22) (2003) 3557–68.
- [6] R. Buchert, F. Wilke, J. van den Hoff, J. Mester, Improved statistical power of the multilinear reference tissue approach to the quantification of neuroreceptor ligand binding by regularization, *J. Cereb. Blood Flow Metab.* 23 (5) (2003) 612–620.
- [7] A. Joshi, J. A. Fessler, R. A. Koeppe, Improving PET receptor binding estimates from Logan plots using principal component analysis, *J. Cereb. Blood Flow Metab.* 28 (4) (2008) 852–865.
- [8] J. Logan, J. Fowler, N. Volkow, Y. Ding, G. Wang, D. Alexoff, A strategy for removing the bias in the graphical analysis method, *J. Cereb. Blood Flow Metab.* 21 (3) (2001) 307–20.
- [9] Y. Zhou, W. Ye, J. R. Brai, A. H. Crabb, J. Hilton, D. F. Wong, A consistent and efficient graphical analysis method to improve the quantification of reversible tracer binding in radioligand receptor dynamic PET studies, *NeuroImage*, 44 (3) (2009) 661–670.

- [10] C. A. Mathis, Y. Wang, D. P. Holt, G. F. Huang, M. L. Debnath, W. E. Klunk, Synthesis and evaluation of ^{11}C -labeled 6-substituted 2-aryl benzothiazoles as amyloid imaging agents, *J. Med. Chem.* 46 (2003) 2740–2755.
- [11] J. Logan, J. S. Fowler, N. D. Volkow, A. P. Wolf, S. L. Dewey, D. J. Schlyer, R. R. MacGregor, R. Hitzemann, B. Bendriem, S. J. Gatley, Graphical analysis of reversible radioligand binding from time-activity measurements applied to $[\text{N-}^{11}\text{C-methyl-}(-)\text{-cocaine}]$ PET studies in human subjects, *J. Cereb. Blood Flow Metab.* 10 (1990) 740–747.
- [12] J. J. Frost, K. H. Douglass, H. S. Mayberg, R. F. Dannals, J. M. Links, A. A. Wilson, H. T. Ravert, W. C. Crozier, H. N. J. Wagner, Multicompartmental analysis of $[\text{}^{11}\text{C}]$ -carfentanil binding to opiate receptors in humans measured by positron emission tomography, *J. Cereb. Blood Flow Metab.* 9 (1989) 398–409.
- [13] M. Slifstein, M. Laruelle, Models and methods for derivation of in vivo neuroreceptor parameters with PET and SPECT reversible radiotracers, *Nucl. Med. Biol.* 28 (2001) 595–608.
- [14] R. N. Gunn, S. R. Gunn, F. E. Turkheimer, J. A. D. Aston, V. J. Cunningham, Positron emission tomography compartmental models, *J. Cereb. Blood Flow Metab.* 21 (2001) 635–652.
- [15] K. R. Godfrey, *Compartmental Models and Their Application*, Academic Press, 1983.
- [16] J. C. Price, W. E. Klunk, B. J. Lopresti, X. Lu, J. A. Hoge, S. K. Ziolko, D. P. Holt, C. C. Meltzer, S. T. DeKosky, C. A. Mathis, Kinetic modeling of amyloid binding in humans using PET imaging and Pittsburgh compound-B, *J. Cereb. Blood Flow Metab.* 25 (11) (2005) 1528–1547.
- [17] R. N. Gunn, A. A. Lammertsma, S. P. Hume, V. J. Cunningham, Parametric imaging of ligand-receptor binding in PET using a simplified reference region model, *NeuroImage* 6 (4) (1997) 279–287.
- [18] H. Guo, K. Chen, R. A. Renaut, E. M. Reiman, Reducing the noise effects in logan graphic analysis for PET receptor measurements, in: proceedings of the 2009 IEEE/CME International Conference on Complex Medical Engineering, accepted.
- [19] M. Yaqub, N. Tolboom, R. Boellaard, B. N. M. van Berckel, E. W. van Tilburg, G. Luurtsema, P. Scheltens, A. A. Lammertsma, Simplified parametric methods for $[(^{11}\text{C})\text{PIB}]$ studies, *Neuroimage* 42 (2008) 76–86.
- [20] S. G. Mueller, M. W. Weiner, L. J. Thal, R. C. Petersen, C. R. Jack, W. Jagust, J. Q. Trojanowski, A. W. Toga, L. Beckett, Ways toward an early diagnosis in Alzheimer’s disease: The Alzheimer’s disease neuroimaging initiative (ADNI), *Alzheimer’s Dement.* 1 (1) (2005) 55–66.
- [21] I. Gradshteyn, I. M. Ryzhik, D. Zwillinger, A. Jeffrey, *Table of integrals, series, and products*, 6th Edition, Academic Press, 2000.